The *Tetrahymena bcd1* mutant implicates endosome trafficking in ciliate, cortical pattern formation

Eric S. Cole[a,*], Wolfgang Maier[b], Ewa Joachimiak[c], Yu-yang Jiang[d], Chinkyu Lee[e], Erik Collet[f], Carl Chmelik[a], Daniel P. Romero[g], Douglas Chalker[h], Nurudeen K. Alli[h], Tina M. Ruedlin[h], Courtney Ozzello[i], and Jacek Gaertig[e]

[a]Biology Department, St. Olaf College, Northfield, MN 55057; [b]Bioinformatics Group, Department of Computer Science, University of Freiburg, 79110 Freiburg, Germany; [c]Laboratory of Cytoskeleton and Cilia Biology, Nencki Institute of Experimental Biology of Polish Academy of Sciences, 02-093 Warsaw, Poland; [d]Molecular Genetics and Cell Biology, The University of Chicago, Chicago, IL 60637; [e]Department of Cellular Biology, University of Georgia, Athens, GA 30605; [f]Department of Cell and Developmental Biology, University of Colorado Anschutz Medical Campus, Aurora, CO 80045; [g]Department of Pharmacology, University of Minnesota, Minneapolis, MN 55455; [h]Department of Biology, Washington University in St. Louis, St. Louis, MO 63021; [i]Molecular, Cellular, and Developmental Biology, University of Colorado Boulder, Boulder, CO 80309

ABSTRACT **Ciliates, such as *Tetrahymena thermophila,* evolved complex mechanisms to determine both the location and dimensions of cortical organelles such as the oral apparatus (OA: involved in phagocytosis), cytoproct (Cyp: for eliminating wastes), and contractile vacuole pores (CVPs: involved in water expulsion). Mutations have been recovered in *Tetrahymena* that affect both the localization of such organelles along anterior–posterior and circumferential body axes and their dimensions. Here we describe *BCD1*, a ciliate pattern gene that encodes a conserved Beige-BEACH domain–containing protein a with possible protein kinase A (PKA)-anchoring activity. Similar proteins have been implicated in endosome trafficking and are linked to human Chediak–Higashi syndrome and autism. Mutations in the *BCD1* gene broaden cortical organelle domains as they assemble during predivision development. The Bcd1 protein localizes to membrane pockets at the base of every cilium that are active in endocytosis. PKA activity has been shown to promote endocytosis in other organisms, so we blocked clathrin-mediated endocytosis (using "dynasore") and inhibited PKA (using H89). In both cases, treatment produced partial phenocopies of the *bcd1* pattern mutant. This study supports a model in which the dimensions of diverse cortical organelle assembly-platforms may be determined by regulated balance between constitutive exocytic delivery and PKA-regulated endocytic retrieval of organelle materials and determinants.**

Monitoring Editor
Wallace Marshall
University of California, San Francisco

Received: Nov 9, 2022
Revised: Mar 15, 2023
Accepted: May 1, 2023

This article was published online ahead of print in MBoC in Press (http://www.molbiolcell.org/cgi/doi/10.1091/mbc.E22-11-0501) on May 10, 2023.

Conflict of interest: There is no conflict of interest.

*Address correspondence to: Eric S. Cole (colee@stolaf.edu or carljchmelik@gmail.com).

Abbreviations used: AKAP, A-kinase–anchoring protein; BCD, broadened cortical domain; BEACH, Beige and Chediak–Higashi; CRN, coronin; CVP, contractile vacuole pore; Cyp, cytoproct; EE, early endosome; LE, late endosome; OA, oral apparatus; OP, oral primordium; PKA, protein kinase A; RAB, Ras-associated binding protein; UM, undulating membrane

INTRODUCTION

Pattern formation in the embryos of multicellular/multinucleate organisms typically involves the generation of morphogen gradients that drive differential gene expression. In this multicellular paradigm, spatial patterns of differentiated cell types are established through the control of transcriptional and translational profiles from individual nuclei at defined locations. Morphogen concentrations represent the input for such patterning mechanisms, whereas differential gene expression is the output.

In contrast, structurally complex unicellular organisms such as ciliates create pattern not through spatial control of emerging cell types, but through assembly of cortical organelles at precise geometric locations around the cell surface (Cole and Gaertig, 2022).

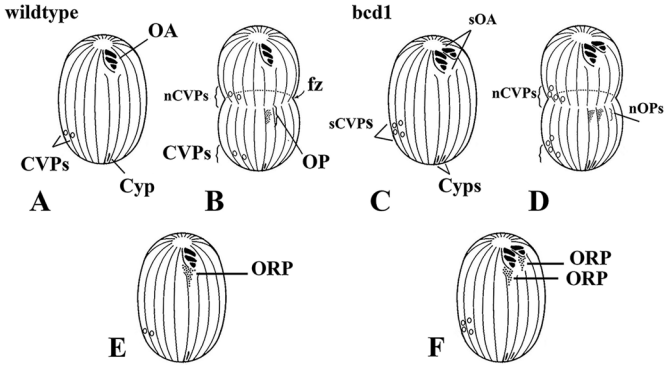

FIGURE 1: Cortical development in the ciliate *T. thermophila*. Vertical lines depict rows of ciliated basal bodies. (A–D) Cortical development during vegetative growth that leads to cell division in nutrient-rich environments in WT and *bcd1* mutant cell lines. (E, F) Alternative developmental pathway that cells exhibit during nutrient deprivation: "Oral Replacement." (A) WT cell depicted with the mature OA, the typical pair of CVPs, and the single Cyp. (B) WT cell undergoing cortical development leading to cell division. The new mouth forms through basal body proliferation within the OP just posterior to the fission zone (fz). New CVPs (nCVPs) form to the viewer's left of the OP and anterior to the fz. (C) A *bcd1* mutant cell exhibiting supernumerary OAs (sOAs) and CVPs (sCVPs) as well as an extra Cyp. (D) Broadened cortical domains as they assemble during predivision cortical development. (E) WT cell under starvation conditions with an oral replacement field (ORP). Basal bodies proliferate just posterior to the mature mouth, partly from the anterior-most region of the stomatogenic kinety and partly from basal bodies that disassemble from the mature UM. (F) Oral replacement observed in *bcd1* cells even under nutrient-rich conditions. The ORP also shows evidence of broadening.

Such cortical patterns reveal the existence of mechanisms that establish anterior–posterior, dorsal–ventral and even left–right asymmetries, just as one sees in the metazoan embryo, yet ciliates execute these patterning processes under the transcriptional power of a single nucleus within a continuous cytoplasmic arena.

The cortex of the ciliate *Tetrahymena thermophila* is highly organized (Figure 1A). A typical cell has 19–21 ciliary rows or "kineties" that run longitudinally from anterior to posterior. At the anterior end of each cell is an oral apparatus (OA). This organelle serves as the mouth and is composed of three membranelles (triple rows of cilia) that form microbe-capturing "combs," and a fourth, "undulating membrane" (UM), that curves from the upper left of the food-capturing aperture (viewer's left) to the lower right. These four membranelles give *Tetrahymena* its generic name. During growth, a new oral primordium (OP) forms in what will become the posterior division-product (Figure 1B). The OP consistently forms along the ciliary row that gave rise to the mature OA in the previous cell division. This establishes the first postoral ciliary row (or "stomatogenic kinety") as a significant, midventral landmark in the circumferential cortical landscape. At the posterior end of each cell, also alongside the stomatogenic kinety, the cell assembles a cytoproct (Cyp). This is the terminal destination of phagosomes or food vacuoles. Phagosomes initially fill with particles collected by the beating ciliated membranelles within the OA. Lysosomes fuse with phagosomes, contributing digestive enzymes and lowering the internal pH in ways suitable for digestion. After depletion of nutrients, the undigested contents of mature phagosomes are expelled by vacuole-fusion with the Cyp, a specialized cortical dock at the posterior end of the cell. Finally, to the cell's right (viewers' left) of the stomatogenic kinety, and in the cell posterior, one finds the contractile vacuole system. This involves a membranous water-expulsion organelle that, upon filling, transiently fuses with another pair of cortical docks, the contractile vacuole pores (CVPs; Figure 1).

A typical wild-type (WT) cell has a single pair of CVPs, though occasionally one or three may be observed. All of these cortical organelles, the OA, the Cyp, and the CVPs, represent sites of active membrane trafficking. At the OA, novel membrane is delivered to assist in phagosome formation (Baumert *et al.*, 1998). At the Cyp, depleted phagosomes dock, fuse, and expel their contents. Water is discharged through fusion of the contractile vacuole with the cortical CVPs. That said, the form and function of each organelle are quite distinct.

In the 1980s and 1990s, a rich collection of ciliate pattern mutants was generated by chemical mutagenesis and visual screening (see Frankel, 2008, for a review). Next-generation genome sequencing has begun to identify the genes involved in ciliate patterning, especially along the anterior–posterior axis (see Cole and Gaertig, 2022, for a review), but until now there has been little insight into mechanisms that regulate circumferential patterning. Circumferential patterning involves the precise placement of cortical organelles (mouth, CVPs, and Cyp) along specific cortical meridians and the control of their lateral dimensions. To gain deeper mechanistic insights into the control of circumferential pattern, we revisited the *bcd1* mutation.

The *bcd1* mutation, first described in 1987 (Cole *et al.*, 1987), produces cells in which cortical organelle domains have been laterally enlarged (broadened cortical domains). Here we describe the identification of the *BCD1* gene by whole-genome sequencing. *BCD1* encodes a protein with a highly conserved Beige/BEACH domain. Metazoan Beige/BEACH-containing proteins have been implicated in lysosome biosynthesis and in the vesicle fission/fusion events that are associated with endosome trafficking (Cullinane *et al.*, 2013; Sharma *et al.*, 2020). They have also been identified as belonging to a family of protein kinase A (PKA)-anchor proteins, or AKAPs (Wang *et al.*, 2000, 2001). We confirmed the identity of the *BCD1* gene candidate by creating strains in which the WT locus was deleted, resulting in the familiar *bcd1* phenotype. Furthermore, sequencing two independently generated (noncomplementing) mutant alleles (*bcd1-1* and *bcd1-2*) identified point mutations at the same chromosomal locus. Bcd1:GFP-tagged cell lines revealed cortical localization associated with the OA, ciliary pockets, basal bodies, and their neighboring parasomal sacs (sites of endocytic activity). We demonstrate that *bcd1* mutants exhibit reduced pinocytosis and phagocytotic activities. We propose and test a hypothesis that Bcd1-mediated control of endosome trafficking is a major contributor to the dimensional regulation of cortical organelle assembly platforms during development. This represents the first ciliate pattern gene identified that plays a significant role in circumferential patterning, in this case defining the lateral dimensions of cortical organelles.

RESULTS

Identifying the *BCD1* gene

The *bcd1-1* mutation was originally mapped to the right arm of micronuclear chromosome 3 using complementation tests in crosses to nullisomic strains lacking specific micronuclear chromosomes (Bruns *et al.*, 1983; Cole *et al.*, 1987). We used "allelic composition contrast analysis" (ACCA) (Jiang *et al.*, 2017) to map the causal mutation for *bcd1-1* (see *Materials and Methods*). Briefly, we sequenced pooled genomes of F2 progeny that were homozygous for either the *bcd1-1* or WT alleles. For each sequence variant, scores were computed that reflect the extent of linkage to the mutant phenotype, and these were plotted against genomic coordinates of the five micronuclear chromosomes. A peak of increased linkage was apparent on chromosome 3 around a ~26 Mb position (Figure 2A).

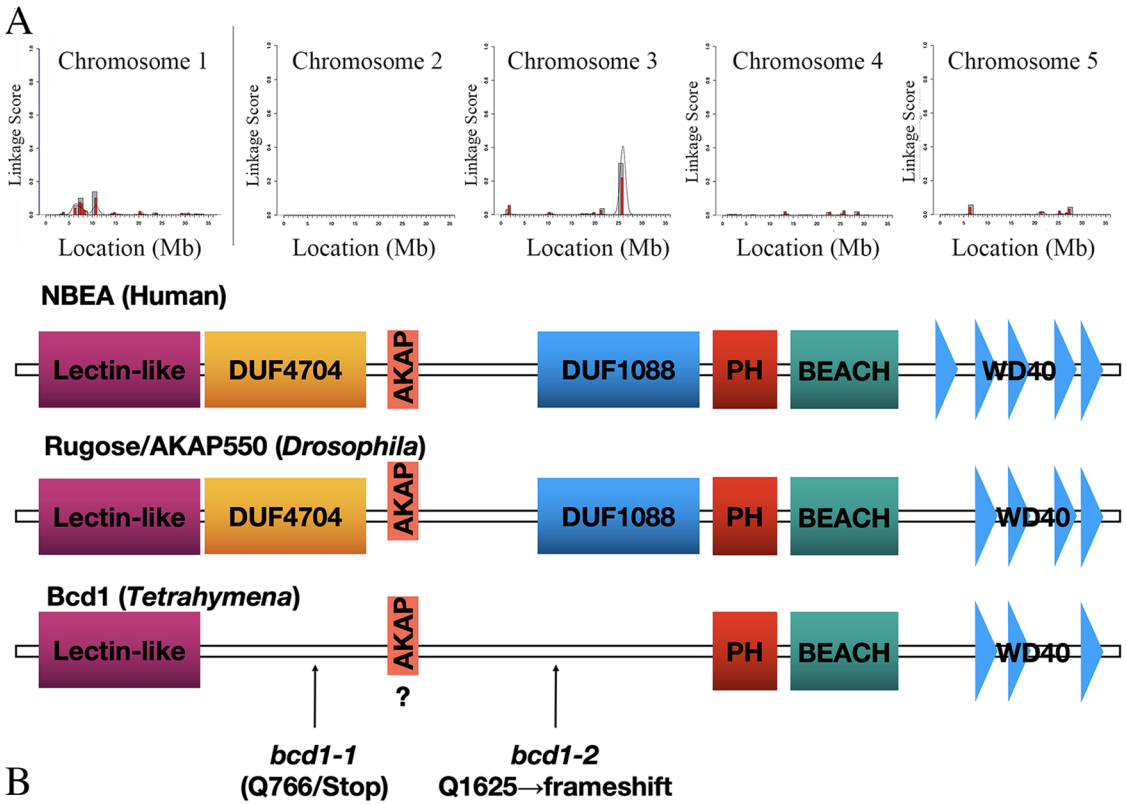

FIGURE 2: *BCD1* alleles map to *TTHERM_00637770*, a gene that encodes a conserved BEACH domain protein. (A) Mapping the *bcd1-1* mutation using the ACCA workflow of comparative whole-genome sequencing (see *Materials and Methods*). The scores reflect the degree of linkage of sequence variants to *bcd1-1* among the meiotic F2 segregants. Note increased linkage signal on chr 3 around the position 26 Mb. (B) Comparison of the domain organization of TTHERM_00637770/BCD1 and its likely orthologues: human NBEA and rugose/AKAP550 of *D. melanogaster*. Approximate positions of the following domains are shown: lectin-like (also known as PFAM laminin_G_3); DUF4704, PFAM domain of unknown function 4704; DUF1008 PFAM domain of unknown function 1088; PH, PFAM PH_BEACH domain; BEACH, PFAM BEACH domain; WD40, WD40 repeats domain. The PFAM domains were detected using SMART (Letunic *et al.*, 2015). The possible PKA-binding motif was located in NBEA based on Wang *et al.* (2000). The lectin-like domain was detected by Phyre2 searches that revealed (Kelley *et al.*, 2015) a lectin-like fold previously described by Burgess *et al.* (2009).

Within this genomic region, there is a single homozygous variant, T to C (chr3:25967103). In the macronucleus, this variant corresponds to an A to G change at chr_114:3259 within the predicted coding region of the *TTHERM_00637770* gene. Augustus gene annotation (Stanke *et al.*, 2006) predicts that *TTHERM_00637770* encodes a large protein composed of 3203 amino acids and the *bcd1-1* linked variant introduces a premature stop codon (TAA Q766 codon changes to a TGA), which results in a large truncation of the predicted protein product. It should be noted that *Tetrahymena* utilizes only one stop codon, UGA; the other two, UAA and UAG, have been reassigned to encode the amino acid glutamine.

BLASTp searches revealed that the TTHERM_00637770 protein has portions of strong amino acid sequence homology to the conserved BEACH (Beige and Chediak-Higashi) domain–containing proteins (reviewed in Cullinane *et al.*, 2013). Within the most C-terminal region of ~800 amino acids, the predicted amino acid sequence TTHERM_00637770 is ~30% identical (50% similar) to the corresponding regions of human BEACH proteins including human NBEA (neurobeachin) (Wang *et al.*, 2000) and its *Drosophila* orthologue rugose/DAKAP550 (Shamloula *et al.*, 2002; Volders *et al.*, 2012). Reverse BLASTp searches using either NBEA or rugose against the predicted proteome of *Tetrahymena* all identified TTHERM_00637770 as the top match.

A second mutation conferring essentially the same "broad-cortical-domain" phenotype maps to the same chromosome arm and fails to complement the *bcd1-1* mutation. This was designated the *bcd1-2* allele. PCR and sequence analysis demonstrated that the *TTHERM_00637770* locus of the *bcd1-2* mutant contains an A to G variant within intron 11 (see Supplemental Figure 1). We hypothesized that this generates a premature splice site 11 base pairs upstream of the predicted WT splice site. Reverse transcriptase-PCR–based sequencing of the *bcd1-2* mRNA confirmed the presence of a gained splice site at that position, resulting in a translational frameshift near the midpoint of the coding region of *TTHERM_00637770*. The *bcd1-1* and *bcd1-2* mutations both result in a truncation of large portions of the protein, including the entire highly conserved C-terminal region, suggesting that *bcd1-1* and *bcd1-2* are null alleles.

To further validate *TTHERM_00637770* as the *BCD1* locus, we targeted a portion of the coding region of *TTHERM_00637770* (from exon 3 to exon 6) for deletion using a scan RNA–based "codeletion" approach (Hayashi and Mochizuki, 2015). Two codel transformant clones carrying deletions within *TTHERM_00637770* were evaluated by immunofluorescence using anti-centrin and anti-fenestrin antibodies to image the cortical organelle patterns. These displayed the *bcd1*- cortical phenotypes, including an increase in the size of

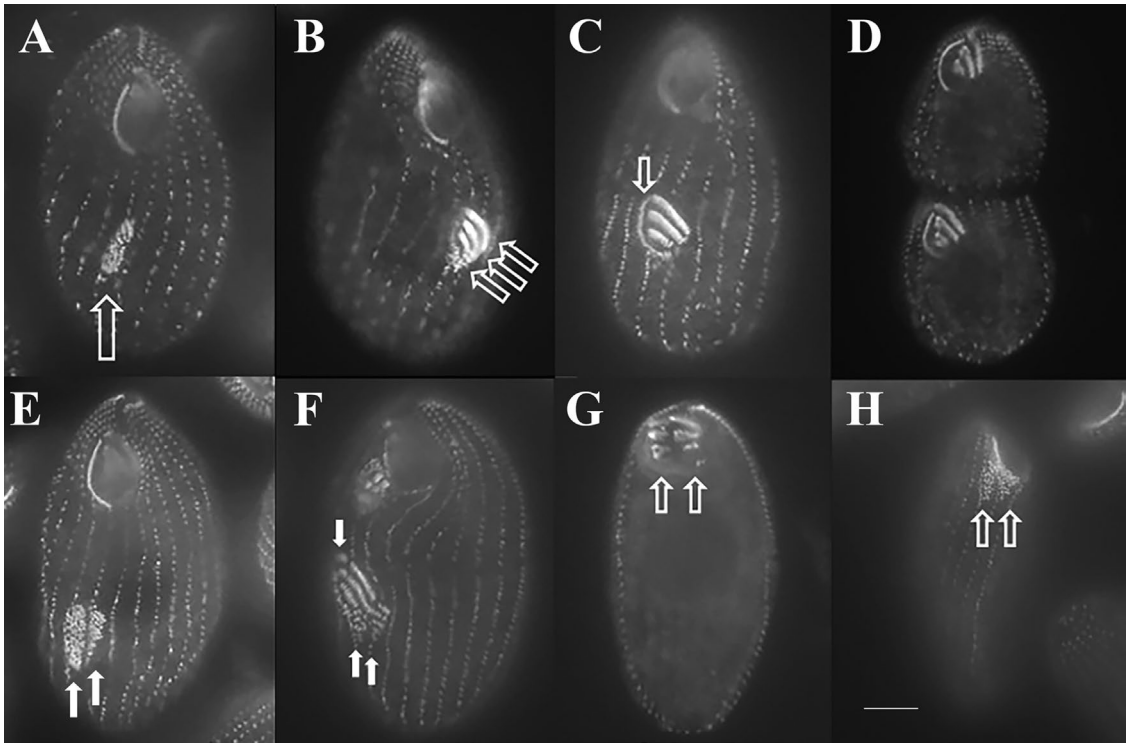

FIGURE 3: Cells labeled with an anti-centrin antibody. (A) WT cell (strain SB1969) in which a single kinety has initiated basal body proliferation launching predivision oral development (open arrow). (B) Later stage WT cell showing organization of basal bodies into three "membranelles" (arrows). (C) Appearance of the UM (arrow). (D) WT cell completing oral development before cell division. (E–H) *bcd1-2* mutant cells. Similar features were seen in *bcd1-1*, *bcd1-2*, and codeletion strain Δ *2* cells. (E) *bcd1* mutant with two adjacent kineties involved in basal body proliferation (arrows). (F) *bcd1-2* mutant cell with three adjacent OPs beginning to organize (and integrate) their membranelles. (G) *bcd1-2* cell in which two adjacent mature OAs have failed to integrate. (H) Mature cell in which "oral replacement" has been initiated. Two fields of proliferating basal bodies can be seen along kineties, just below the compound OA that is beginning to disassemble (open arrows). Scale bar = 10 μm.

oral and CVP cortical domains (see below). All these data led to a strong conclusion that *TTHERM_00637770* is *BCD1*.

A comparison of Bcd1 to NBEA and rugose reveals two regions of amino acid sequence homology near the C- and N-termini (Figure 2B and Supplemental Figure 2). Within the C-terminal region, all three proteins have a PH (pleckstrin homology) domain and a BEACH domain followed by multiple WD40 repeat domains. In NBEA and rugose, the conserved N-terminal region contains a Laminin_G-3 PFAM domain, but such a domain was not detected in *BCD1*. However, Phyre2 searches (Kelley *et al*., 2015) predicted with high confidence that this region has a fold also present in domains of sialidase B of *Streptococcus pneumoniae* (PDB:2JKB), tetanus toxin (PDB:5N0C; Masuyer *et al.*, 2017), and laminin α2 chain G-like module (PDB:1QU0; Hohenester *et al.*, 1999). As suggested, these domains have a lectin-like fold that could be involved in the oligosaccharide binding in the secretory pathway (Burgess *et al*., 2009). Some animal BEACH domain proteins, including NBEA and rugose, function as AKAPs through PKA-binding motifs. Amino acid regions involved in binding of the RII regulatory PKA subunit were mapped in rugose (Han *et al*., 1979) and NBEA (Wang *et al*., 2000). Bcd1 colinear regions exhibit weak similarity to the PKA-binding motifs reported for both rugose and NBEA (Supplemental Figure 2). Thus, Bcd1 may have a divergent AKAP motif, or lack this entirely.

The cortical phenotype

The original studies on the *Tetrahymena bcd1* mutants analyzed their cortical pattern phenotype using classical silver-staining methods (Frankel and Heckmann, 1968; Nelsen and DeBault, 1978). The molecular targets of silver staining are ill defined but loosely correlate with the cortical, microtubule architecture. We revisited these phenotypes using a defined monoclonal antibody, 20H5 (Sanders and Salisbury, 1995), that recognizes the conserved basal body component centrin and with the GFP- and mCherry-tagged (Fen1) proteins that decorate the CVPs, Cyps, and other cortical apertures (Cole *et al*., 2008). One of the more extreme elements of the *bcd1* phenotype involves the OA (Figure 3). In WT cells, a field of basal bodies proliferate from a small subset of ciliated basal bodies located at midbody alongside the "stomatogenic kinety" (Figure 1B). This field of proliferating basal bodies becomes organized into the daughter cell's OP. In *bcd1* mutants, the oral domain can be enlarged, manifesting as a single OP with laterally elongate membranelles or, in more extreme cases, adjacent ciliary rows are recruited to propagate basal bodies which are then assembled into multiple, side-by-side OAs (Figures 1D and 3, E–G). The resultant mutant OA may be defective, as indicated by reduced food vacuole formation (see below) and by the high incidence of "oral replacement" (ORP), a physiological response typically triggered in *Tetrahymena* cells by starvation (Frankel, 1969; Nelsen, 1978). ORP involves resorption of the mature OA and basal body proliferation along the postoral kinety joining basal bodies from the disassembling UM to build a new oral replacement field. When cells were raised under nutrient-rich conditions, we saw no WT cells undergoing ORP, while 10% of the Δ2 strain, 15% of the *bcd1-1* strain, and 22% of the *bcd1-2* strains were undergoing ORP ($N = 100$ for each genotype).

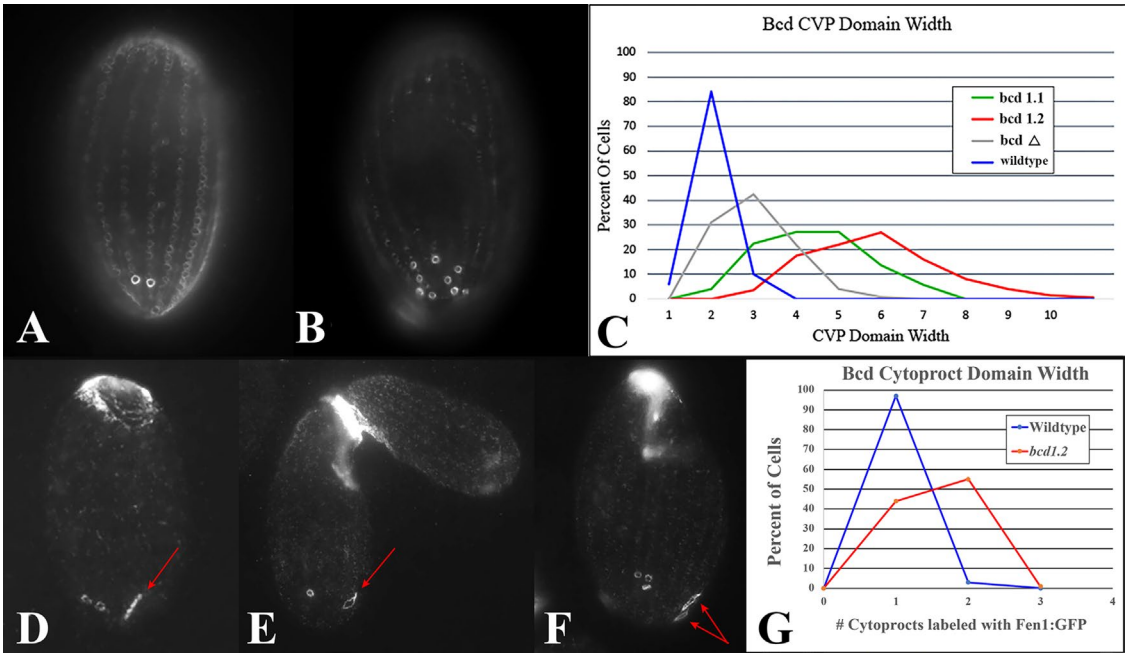

FIGURE 4: CVP and Cyp domain widths in WT and mutant cells. (A) WT cell labeled with Fen1:M-CherryFP. Note a typical pair of CVPs (brightly staining circles). (B) *bcd1-2* mutant cell labeled with Fen1:M-CherryFP. In this example, nine CVPs are labeled. (C) Graph showing distribution of cells with various numbers of CVPs. WT cell = CU428 (blue), mean CVP number for WT = 2.04 ($N = 100$). Codeletion strain (*bcd*Δ) appears in gray). Mean CVP count for *bcd*Δ (codeletion strain) = 3.01 ($N = 100$). CVP distribution for *bcd1-1* and *bcd1-2* shown in green and red, respectively, mean = 4.41 ($N = 250$) and 5.85 ($N = 200$), respectively. Scale bar = 10 μm. (D–G) Fen1:GFP decoration of WT and *bcd1.2* cells during costimulation and conjugation, focusing on the number of each cell's Fen1-decorated Cyps. (D) Starved WT cell showing a pair of CVPs and a single "closed" Cyp (arrow). (E) WT conjugal partner showing its single Cyp in the "open" configuration (arrow). (F) *bcd1.2* cell displaying two Fen-decorated Cyps in partially open configurations (arrows). (G) Distribution of WT and *bcd1.2* mutant cells with 0, 1, 2, and 3 Cyps ($N = 100$ WT and 110 *bcd1.2* cells, respectively).

A more easily quantified aspect of the *bcd1* cortical phenotype is the number of CVPs. WT cells typically have two (±1; see Figure 4A). Using CVP numbers, the *bcd1-2* allele again exhibits the strongest phenotype, followed by *bcd1-1* and then our codeletion strain, co-del Δ2. The same rank order of phenotypic strength was seen using a variety of different measures. Variable penetrance and expressivity of the phenotypes are likely due to differences in genetic background.

We report here, for the first time, that *bcd1* mutants also exhibit broadening of the Cyp domain (Figure 4, F and G). Very few studies have been conducted on this cortical organelle. We examined Fen1:GFP-decorated WT and *bcd1.2* mutant alleles after they had been starved overnight in Tris. WT cells were rarely found with more than one Cyp (3%), but the incidence rose to 56% among *bcd1.2* mutants ($N = 100$). In summary, the *bcd1* mutant phenotype exhibits broadening of all three of the major cortical organelles in *Tetrahymena*, the OA, the CVP domain, and the Cyp domain.

Bcd1 protein localization

The endogenous locus *BCD1* gene was fused to the GFP sequence, and cells expressing Bcd1:GFP were imaged by immunofluorescence with anti-GFP antibodies. Bcd1:GFP fusion protein localized to the cell cortex in rows of punctae associated with ciliary pits and their associated basal bodies (Figure 5), within the oral apparatus, and on various internal, cytoplasmic vesicles. Cortical distribution was conspicuously more abundant at the anterior end of each cell though labeling could be detected along the full length of each cell, especially during cell division. We also observed a subtle "chiral bias" as the more conspicuous protein localization extended more posteriorly along ciliary rows to the cell-left of the stomatogenic kinety. The anterior/posterior (A/P) gradient of Bcd1:GFP metamerizes late during cell division after the fission zone is well established, creating a new high point posterior to the developing fission zone (Figure 5F). As cytokinesis proceeds, a ring of brightly labeled punctae appear just posterior to the fission zone (Figure 5G).

On close examination, these cortical punctae appear as clusters of multiple foci localized around the basal bodies (Figure 5, D and H). With immunogold labeling and transmission electron microscopy (TEM), we observed gold particles over ciliary pits (Figure 5, I and J), basal bodies (especially in the vicinity of the transition zone), and parasomal sacs (Figure 5, K and L). Parasomal sacs are sites of active membrane pinocytosis, found at the base of every cilium.

Exploring membrane trafficking in the *bcd1* mutant

The *bcd1* mutant was originally described solely on the basis of its impact on the cell's cortical cytoskeleton, yet the corresponding gene shows homology to Beige/BEACH-domain–containing proteins associated with membrane trafficking: endosome fission, fusion, and lysosome defects (Cullinane *et al.*, 2013). It seemed prudent to examine our *Tetrahymena bcd1* mutant from the perspective of membrane trafficking.

Phagocytosis. *bcd1 mutants exhibit diminished food vacuole formation*

Bcd1:GFP is localized within the mouth (OA) and along the deep fiber bundle that conducts phagosomes from the buccal cavity into

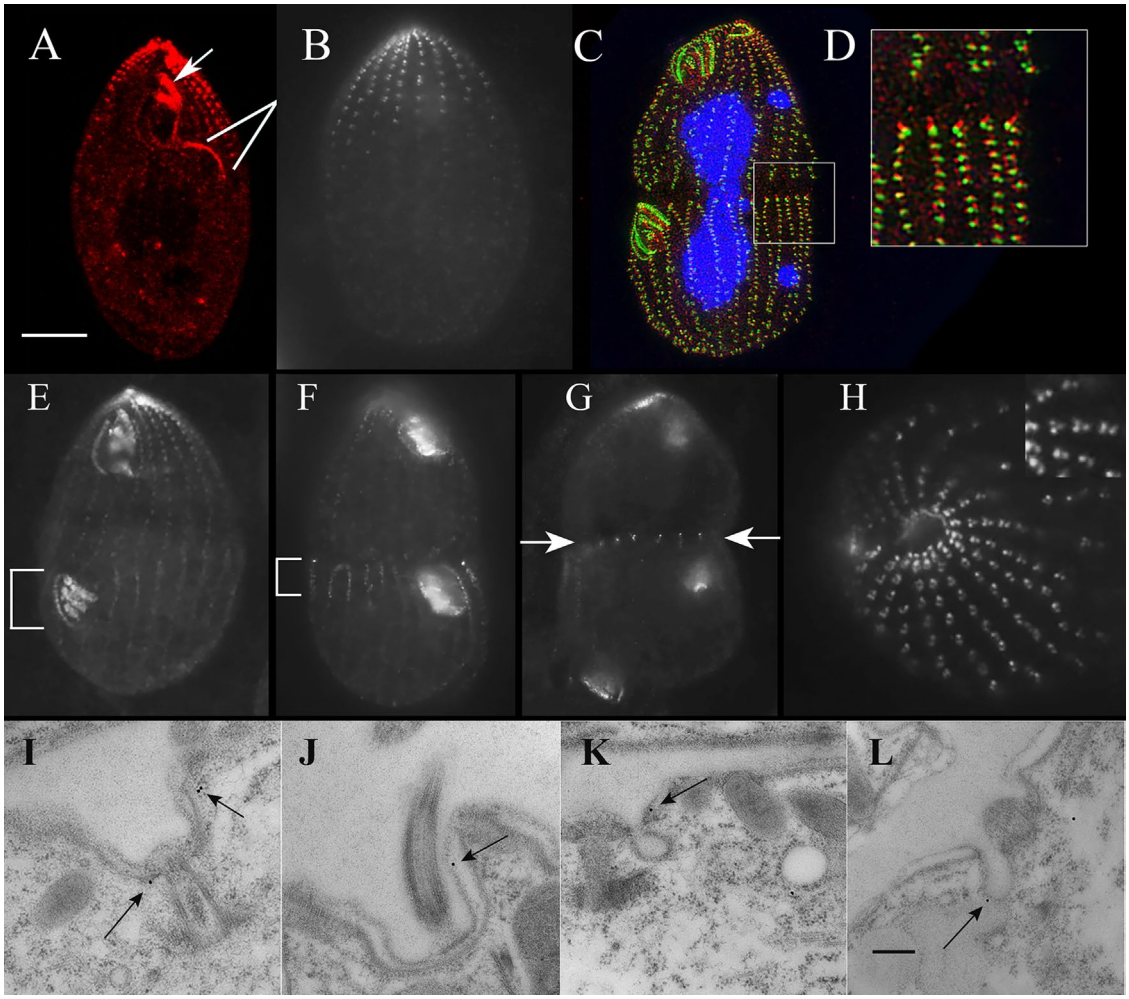

FIGURE 5: Bcd:GFP localization. (A) Bcd:GFP was seen decorating the OA (top arrow) and the deep fiber bundle (a microtubule track that newly formed phagosomes travel). (B) This image highlights both the linear rows of punctae in the anterior cortex and deeper punctae within the cytoplasm (bottom arrows). (C, D) Cortical punctae appear more intensely labeled at the anterior end of the cell associated with ciliated basal bodies and form a spirally distributed gradient, extending most-posterior along the ciliary row just below the OA and reaching less far posterior as one circles to the cell left (viewer's right). The posterior-most "high point" coincides with the location of the developing OP just below midbody (bracket in C). (E) Dividing cell showing intense labeling of both the mature OA and the developing OP at midbody (bracket). Bcd labeling appears more uniform within A/P punctae during early division. (F) As the division furrow proceeds, The Bcd label becomes restricted to punctae just posterior to the fission zone in what will become the new anterior of the posterior division product (establishing a new A/P gradient). (G) Bcd:GFP-labeled punctae become restricted to a single equatorial region just posterior to the fission zone. (H) Close-up of the anterior-most punctae reveals complex clusters of Bcd:GFP-labeled structures. Immunogold TEM reveals ultrastructural localization within the ciliary pocket (I and J) and within the "parasomal sac" just anterior to each basal body (K and L), a cortical site active in pinocytosis.

the cell interior (Figure 5A). *bcd1* mutants also exhibit unusually slow growth. For these reasons we examined rates of feeding between WT, *bcd1-1*, *bcd1-2*, and the codeletion mutant, *bcd1Δ2* (Figure 6, A–D). Cells expressing *bcd1* mutations exhibit a significant reduction in food vacuole formation (phagocytosis) of varying severity, with *bcd1-2* exhibiting the most severe defect and *bcd1Δ2* (codel Δ2) exhibiting the least severe defects. Even in healthy WT cultures, one never sees the entire population feeding at any given time. This is due to the fact that during cytokinesis, the mature OA partially disassembles and is remodeled. In one experiment, 93% of the WT (B2086) population were actively feeding, while 58% of the *BCD1*-deletion strain (codel Δ2) and only 26–27% of the original *bcd1* mutants took up particles over a 15-min interval. Curiously, among individual *bcd1-1* cells that were capable of feeding, the rate of phagosome filling was indistinguishable from that of the feeding WT cells.

Late endosomes/lysosomes. *bcd1 mutants exhibit an overabundance of late endosomes/lysosomes.*

We followed the fate of phagosomes in both WT and mutant cells by labeling lysosomes with *Tetrahymena* Rab7:YFP. Rab7 associates with late endosomes (LEs), possibly as they transition into lysosomes (Bright *et al.*, 2010), and with phagosomes that they later associate and likely fuse with during phagosome maturation. In Rab7:YFP-labeled cells, we distinguished phagosomes from LE/lysosomes based on their larger size and more diffuse labeling. This was confirmed by feeding Rab7:YFP-expressing cells with India ink (Figure 6, I–L). *bcd1-2* mutants exhibited considerably more Rab7:YFP-labeled endosomes that were on average modestly larger than their WT counterparts (0.91 μm for *bcd1-2* vs. 0.74 μm for B2086 WTs; $N = 100$ for each genotype). Curiously, the number of labeled LEs per cell was inversely proportional to the number of phagosomes present. When

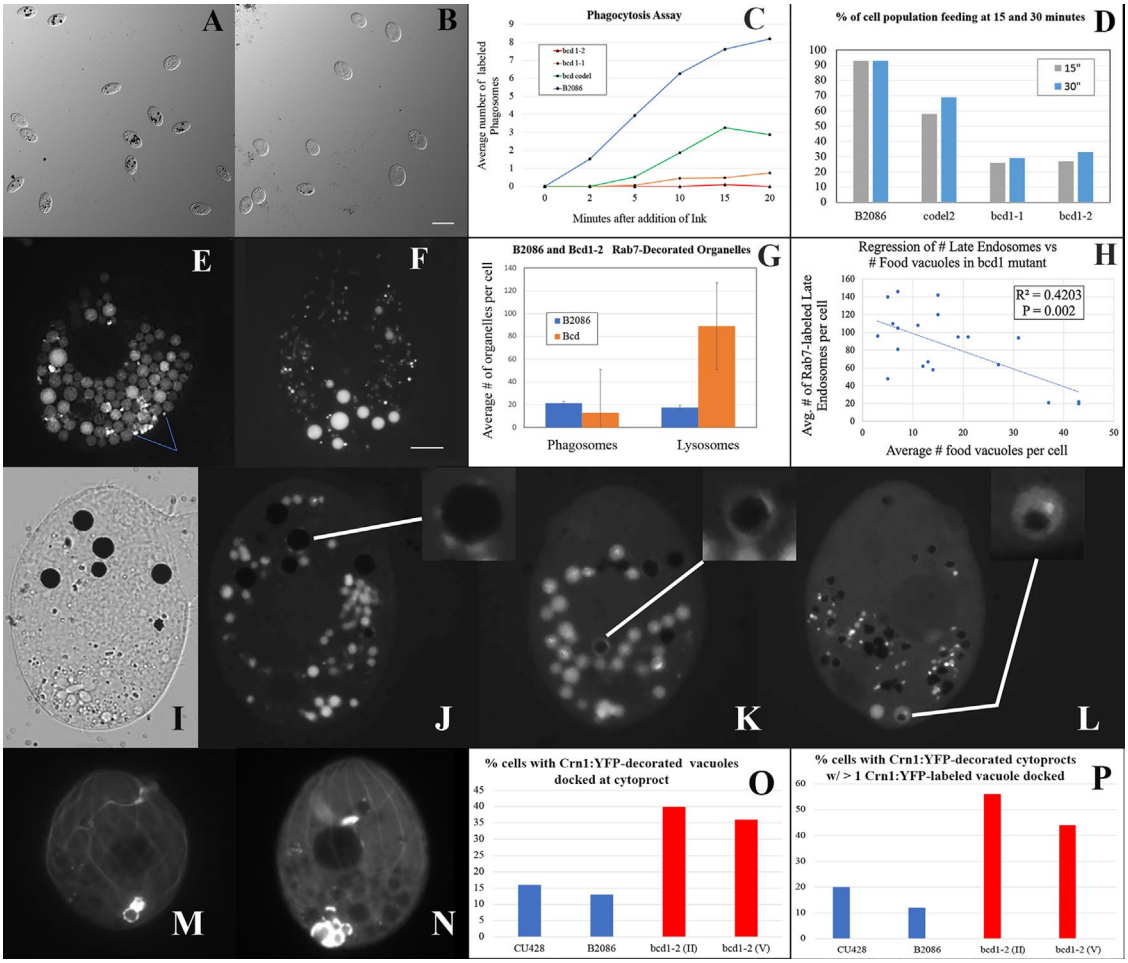

FIGURE 6: Phagosomes, lysosomes, and coronin1-labeled "terminal" phagosomes in *bcd1* and WT cells. (A, B) DIC microscope images of WT (B2086) and *bcd1-2* mutant cells 15 min after addition of India ink. Scale bar = 50 µm. (C) Phagocytosis assay: number of ink-filled phagosomes per cell over time ($N = 150$ for each cell type). (D) Relative proportion of populations taking up food particles ($N = 100$ for each cell type). (E) Rab7:YFP-labeled WT cells (LEs or lysosomes). Larger compartments were identified as food vacuoles (phagosomes); smaller punctae (arrows) were identified as LEs or lysosomes. (F) Rab7:YFP-labeled *bcd1-2* cells. Note more abundant punctae (LEs/lysosomes) and few, yet more brightly labeled, phagosomes. Scale bar = 10 µm. (G) Relative abundance of Rab7:YFP-labeled phagosomes (larger vacuoles) and LEs/lysosomes (smaller vesicles) per cell; $N = 20$ for each genotype. (H) Regression analysis revealing negative correlation between numbers of food vacuoles and numbers of lysosomes in *bcd1-2* mutant cells ($N = 20$). A similar correlation was true of WT cells. (I–L) Images of Rab7:YFP-labeled *bcd1-2* mutant cells fed carmine particles to identify phagosome compartments. Arrows indicate ingested carmine within vacuoles that also decorate with Rab7:YFP. (I, J) Tiny Rab7:YFP-decorated vesicles appear to adhere and possibly fuse with carmine-loaded phagosomes 20 min after feeding (see insert panel J). (K) Phagosome more fully decorated with Rab7YFP 30 min after feeding (see insert). (L) *bcd1.2* mutant cell displaying dark food particles within brightly labeled vacuoles 2 h after feeding. (M) Coronin1 (Crn1):YFP-labeled WT cell. Note Crn1 label over deep fiber of OA (top arrow) and labeled vacuole docked next to egesting Cyp (bottom arrow). (N) Crn1-YFP–labeled *bcd1-2* cell. Note abundance of Crn1-labeled vacuoles docked at the Cyp (arrows). (O) Quantitation of Crn1-decorated Cyps in mutant and WT cell populations ($N = 100$). Most WT cells captured at a given moment do not have a Crn1-labeled vacuole docked for egestion. Note that twice as many *bcd1-2* cells display docked Crn1-vacuoles than their WT counterparts. (P) Percentage of cells that display Crn1-YFP–decorated Cyps, with more than 1 Crn1:YFP-decorated vacuole docked ($N = 100$). Note that more *bcd1-2* cells exhibit supernumerary Cyp-docked vacuoles.

the number of phagosomes (diffusely labeled vacuoles, 2–5 µm in diameter) was plotted against the number of LEs (<1.0 µm diameter, brightly labeled vesicles), we saw a significant negative correlation: the more phagosomes present in a cell, the fewer LEs were present. We hypothesized that without phagosomes serving as trafficking destinations, LEs accumulate in the mutant cell cytoplasm (a "destination failure"). This hypothesis was supported by a similar correlation in WT cells. It may be significant that in mutant cells with fewer phagosomes (Figure 6F), the phagosomes that were present actually labeled more brightly than their WT counterparts, possibly indicating an excess of LE fusion.

Phagosome egestion from the Cyp. *bcd1 mutants accumulate excess, Crn1-labeled phagosomes at the Cyp.*

Coronin-1 is an actin-associated protein implicated in formation and maturation of phagosomes (Yan *et al.*, 2005). Actin localizes around both the OA and the Cyp in *Tetrahymena* (Hirono *et al.*, 1987). Coronins have also been shown to associate with AKAP

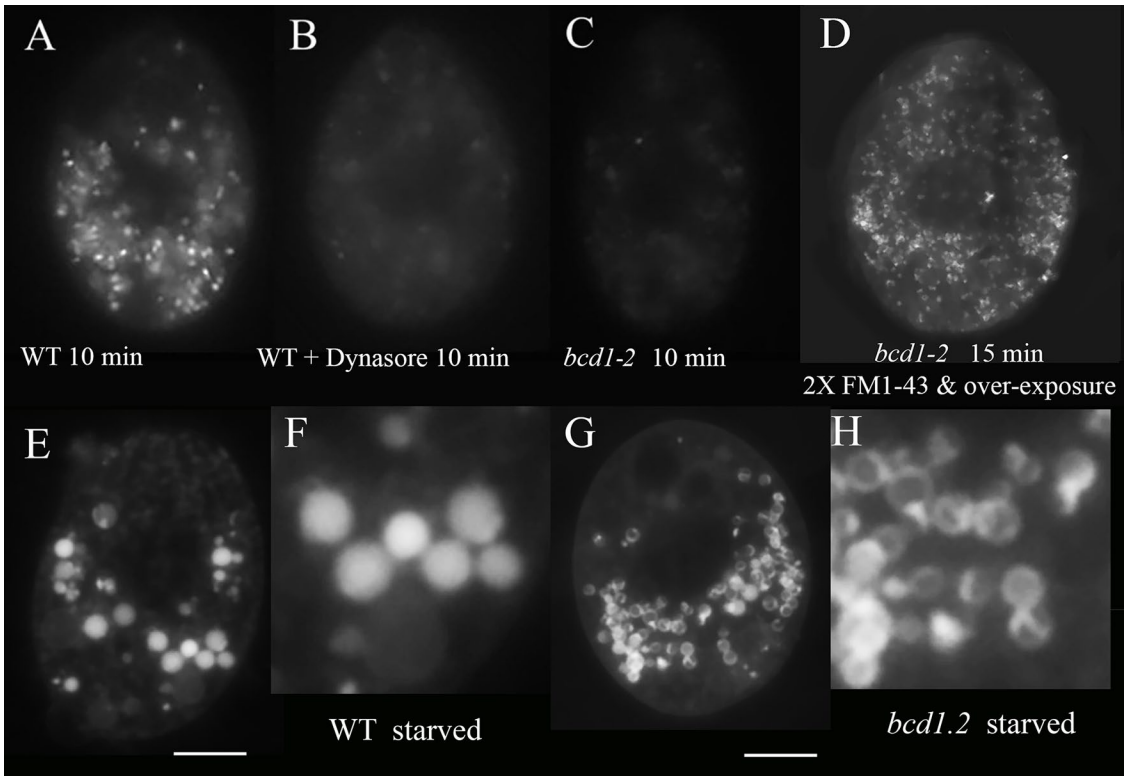

FIGURE 7: Pinosomes in WT and *bcd1* mutant cells and cells treated with dynasore. (A) Fed WT (SB1969) *Tetrahymena* cells labeled for 3 min with 5 mM FM1-43 and photographed 10 min after initial exposure to the FM dye. Vesicles were identified as EEs. (B) The same SB1969 cells treated with 70 μM dynasore 2 h before FM 1-43 labeling. (C) *bcd1-2* mutant cells labeled 3 min with 5 mM FM1-43 and photographed 10 min later. In all three cases, cells were exposed to FM dye for 3 min, washed twice, and imaged 10 min after initial exposure to the dye. All three images were captured using a 100 ms photographic exposure, with no alteration of brightness/contrast of the image. (D) *bcd1-2* cell labeled with 10 mM FM1-43 (2×) for 15 min and photographed using prolonged exposure time. (E, F) WT (B2086) cells starved overnight in 10 mM Tris, pH 7.4 and FM labeled (as for A–C) and photographed 15 min after exposure, showing movement of dye into larger vacuoles. Note uniform labeling of probe. Scale bar = 10 μm. (G, H) *bcd1-2* cells starved overnight in 10 mM Tris, pH 7.4, FM labeled (as for D) and photographed 15 min after exposure, showing movement of dye into curious annular labeling of larger vesicles. Scale bars = 10 μm.

proteins (Benz *et al.*, 2020). We cloned the *Tetrahymena* coronin homologue (TTHERM_00293380) and engineered a fusion-construct with YFP, expressing it in both WT and *bcd1-2* mutant cells (Figure 6, M–P). In the WT, the Crn1:YFP label decorates the deep fiber of the OA (Figure 6M), and large vacuoles immediately adjacent to the Cyp, the cellular site for egestion of "spent" food vacuoles (see Allen, 1984). Watching live cells expressing Crn1:YFP in real time, it became clear that phagosomes in the vicinity of the Cyp become richly decorated with Crn1:YFP just before fusing with this cortical docking site. Following fusion (egestion), the Crn1:YFP signal briefly (intensely) decorates the region around the Cyp and then diffuses or dissipates. At any given time, 10–15% of WT cells have a decorated phagosome docked at the Cyp. This led us to believe that Crn1 is involved not only in the formation of phagosomes at the OA but also in their terminal fusion with the Cyp during egestion. *bcd1-2* cells expressing Crn1:YFP were twice as likely to have Crn1-decorated vacuoles docked at the Cyp (35–40% of the population), where they appeared to accumulate around the site of egestion (Figure 6N). We hypothesize either that *bcd1* mutants exhibit a delay in phagosome fusion/egestion causing accumulation of excess phagosomes or, with supernumerary Cyps assembled at the cell cortex, more food vacuoles might be "captured," thereby elevating the number of cells exhibiting docked vacuoles at any given time.

To summarize, *bcd1* mutants show a reduction in phagocytosis, resulting in cells with fewer than the normal number of phagosomes. This correlated with an overabundance of LE/lysosomes. We propose that LE/lysosomes accumulate in the cytoplasm due to reduction of this destination compartment ("destination failure"). We also observed an excess of Crn1-labeled, "terminal" phagosomes in the *bcd1* mutant, accumulating at the Cyp or site of phagosome egestion. This suggests either a delay in late-phagosome fusion with the Cyp or an excess of phagosome docking behavior as a consequence of the cell assembling supernumerary Cyps.

Pinocytosis and early endosomes. *bcd1 mutants show a paradoxical reduction in pinocytosis activity, yet oveabundance of early endosomes.*

FM 1-43 is a water-soluble dye used to fluorescently label pinosomes delivering surface membrane and extracellular materials into the cell interior via dynamin-mediated endocytosis (Elde *et al.*, 2005). In *Tetrahymena*, pinosome endocytosis occurs at highly stereotyped locations, parasomal sacs, located just anterior to each basal body and within the "ciliary pocket." Clathrin-coated vesicles derived from these parasomal sacs have been shown to fuse with early endosomes (EEs) (Allen, 1967; Allen and Fok, 1993). We performed FM 1-43 labeling of WT cells (strain SB1969 or B2086) exposed for 2 h to 70 μM dynasore (a dynamin-specific, GTPase inhibitor) and *bcd1-2* mutants

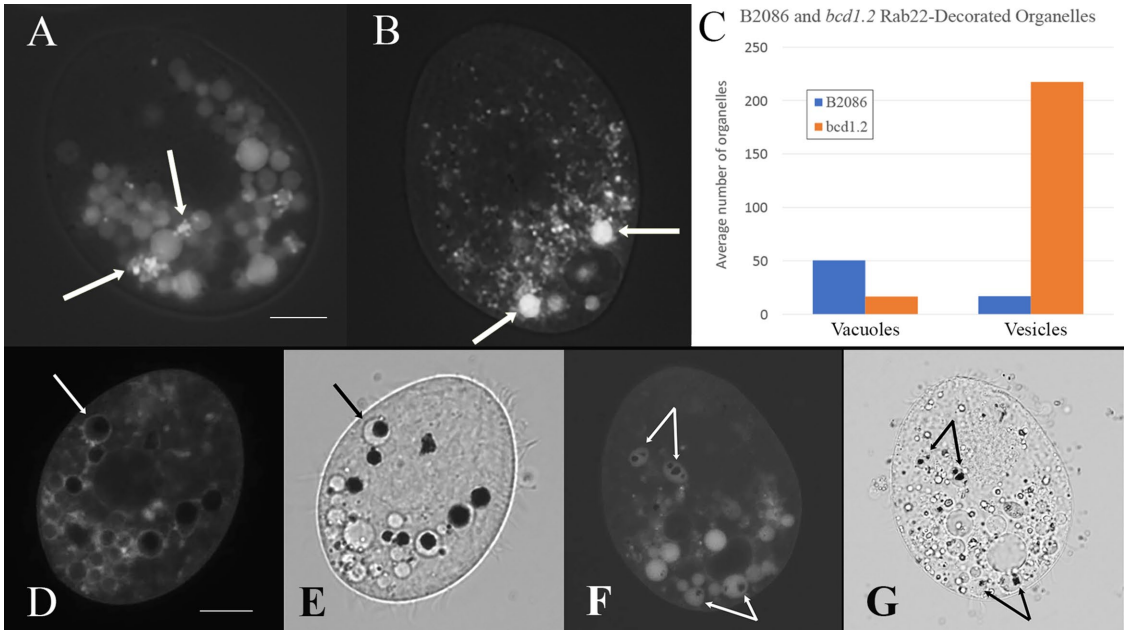

FIGURE 8: EEs. Rab22:GFP-labeled cell lines. (A) WT (B2086) cell induced to express a GFP-tagged *Tetrahymena* homologue to Rab22 associated with EEs (Bright *et al.*, 2010). Arrows point to clusters of small vesicles (likely EEs) surrounded by larger, Rab22-labeled vacuoles (likely phagosomes). (B) *bcd1-2* cell induced to express the Rab22:GFP fusion gene. Arrows indicate brightly labeled (scarce) large vacuoles (likely phagosomes) against a background of abundant smaller vesicles (likely EEs). Scale bar = 10 µm. (C) Relative proportions of Rab22-labeled vacuoles to vesicles in mutant (orange, $N = 27$) and WT (blue, $N = 23$) cells. (D) WT (B2086) cells expressing Rab22:GFP and fed carmine particles (black phagosome contents). White arrow indicates fluorescence labeling of small vesicles decorating the periphery of a large, carmine-identified food vacuole or phagosome. Cells were fed 30 min before the photo session. (E) Bright- field image of the same. (F, G) Fluorescence and bright-field imaging of *bcd1.2* cells expressing Rab22:GFP and fed carmine particles (black inclusions). Cells were fed 120 min before the photo session. At this time, dark carmine particles were conspicuous inside phagosomes that were fully "saturated" with Rab22:GFP labeling. Panels D–G validate interpretation of at least some of the larger, Rab22:GFP-labeled "vacuoles" as phagosomes. Scale bars = 10 µm.

(Figure 7). When labeled for 10–15 min, WT cells exhibited an abundance of FM-labeled internal compartments approximately 1 µm in diameter (Figure 7A). Electron micrographs suggest that clathrin-coated pinosomes are less than 200 nm in diameter (Allen, 1967; Elde *et al.*, 2005), so we suspect that the FM-labeled vesicles visible after 10 min of labeling are, in fact, the larger, EEs. WT cells treated with 70 µM dynasore exhibit substantially reduced fluorescence labeling (Figure 7B). *bcd1-2* mutant cell lines also exhibited reduced FM labeling (Figure 7C). The reduced FM-labeled vesicles within *bcd1-2* cells could be imaged by doubling the FM probe concentration and increasing the photographic exposure time (Figure 7D). It would appear that the *bcd1* mutation significantly reduces pinocytotic activity.

The dimly labeled FM-positive compartments of the *bcd1* mutant appeared more abundant and smaller than the brightly labeled endosomes found in WT cytoplasm. Prolonged photographic exposure of WT cells did not reveal a similar elevation of dimly labeled vesicles. In WT cells, FM label quickly appears within larger vacuoles as well. Curiously, cells starved overnight in 10 mM Tris, pH 7.4, exhibit a different pattern of FM labeling (Figure 7, E–H). In starved, WT cells, FM probe appears within large vacuoles within 15 min of exposure (Figure 7, E and F). Labeling appeared uniform over these compartments. In starved *bcd1.2* cells, the probe also became associated with larger vesicles within 15 min, yet the FM probe often created a curious annulate labeling pattern (Figure 7, G and H).

Because one might predict that a FM probe moves directly from pinosomes to EEs, we examined mutant and WT cells expressing Rab22:GFP, a marker which, it has been suggested, decorates this compartment (Bright *et al.*, 2010) (Figure 8). WT cells induced to express Rab22:GFP overnight appeared on average with 16.9 labeled small vesicles (hypothesized to be EEs) and 50.4 labeled larger vacuoles (suspected phagosomes or food vacuoles; Figure 8, A–C). This likely represents the steady-state condition and suggests that Rab22 either decorates both EEs and phagosomes or that Rab22 moves from the EEs into the phagosomes during phagosome maturation. We confirmed the "phagosome" identity of the larger vacuoles by feeding Rab22:GFP-expressing cells with carmine particles (Figure 8, D–G). We also observed what appeared to be the smaller EEs docking (fusing?) with phagosomes (Figure 8, D and E, arrow).

The *bcd1-2* mutant exposed in an identical manner revealed brightly labeled EEs, averaging 217.3 per cell with only 16.6 food vacuoles (Figure 8, B and C). Again, the less frequent *bcd1-2* phagosomes appeared to label brightly (Figure 8, B and F), suggesting that they were more frequent targets for fusion by the labeled EEs.

This represents a 12-fold elevation in Rab22-labeled compartments within the mutant (a result similar to that seen with the faint-staining compartments labeled with FM probe during pinocytosis; Figure 7, A and D). Taken together, the FM1-43 probe and Rab22:GFP labeling results suggest that in WT cells, EE materials can be shuttled into developing phagosomes. Under conditions with reduced phagosome production (as seen in the *bcd1* mutant), we see elevated EE abundance. It may be useful to point out that while EE contents are traditionally supplemented by materials derived through pinocytosis, they are fundamentally composed of materials generated through anterograde delivery from the Golgi apparatus (Toh *et al.*, 2017; Tan and Gleeson, 2019). We are

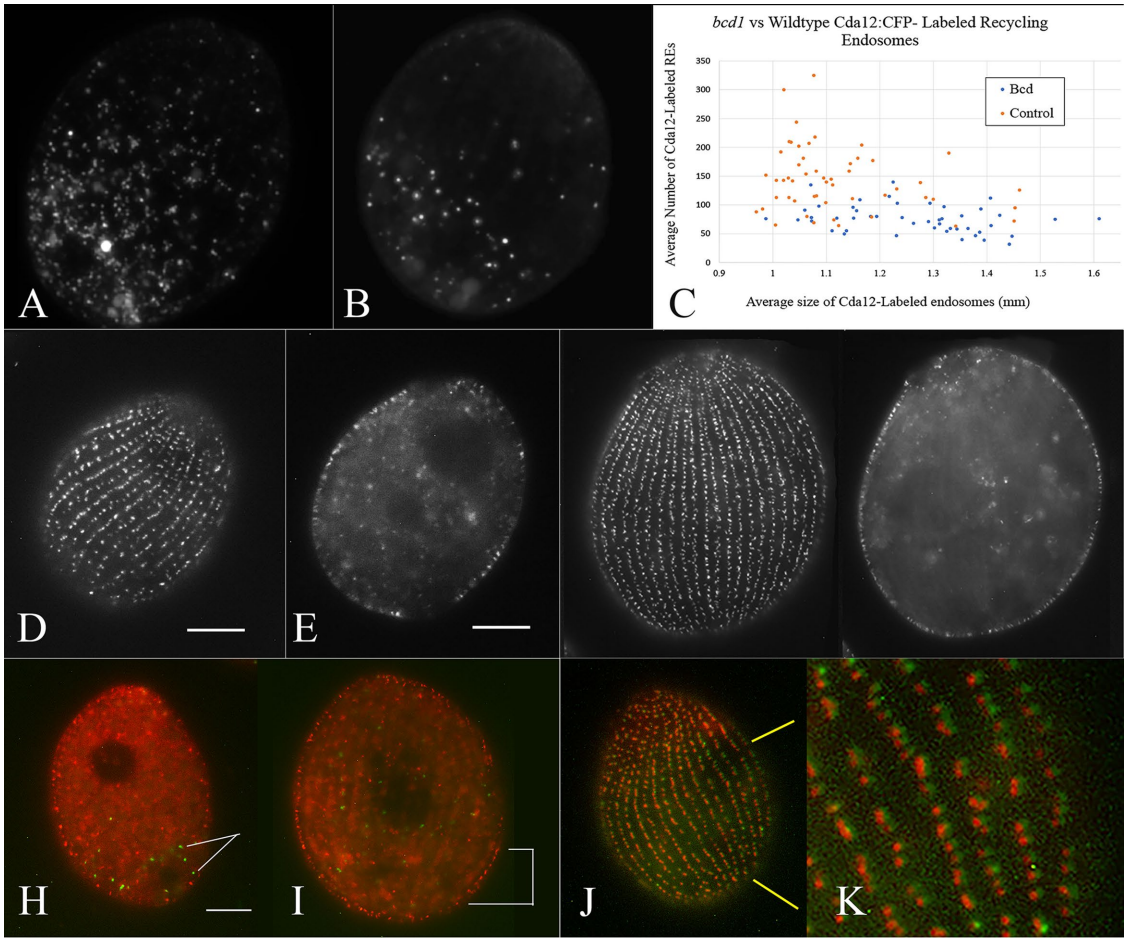

FIGURE 9: Cda12:mCherry-labeled compartments in WT and *bcd1-2* mutant cell lines. (A) WT (CU428) cell line showing cytoplasmic vesicles after 3 h of induced, fusion-gene expression. (B) *bcd1-2* cell line showing Cda12:mCherry labeling after 3 h. (C) Graph illustrating how there are more abundant yet smaller CDA12-labeled vesicles after 3 h in WT (orange) vs. *bcd1-2* (blue) cells ($N = 50$ each genotype). (D, E) WT and (F, G) *bcd1.2* cells labeled with Cda12:mCherry for 18–24 h showing both surface and deep-focus images. One can observe the previously documented overabundance of what appear to be secretory granules. (H–K) WT cells double labeled with Grl1:GFP (granule-lattice protein associated with dense-core secretory granules or mucocysts, green) and Cda12:mCherry (red). (H, I) After just 3–6 h of induced early coexpression, we see what we interpret as developing mucocysts (green, undocked, deep cytoplasmic vesicles labeling, arrows in I) and Cda12-labeled compartments (red, brackets in I). These show little or no colocalization. (J, K) After 18–24 h of coexpression, the mature, docked mucocysts (green) show colocalization with Cda12:mCherry-labeled endosome markers (red).

tempted, once again, to assign the overabundance of EEs to a "destination failure." With fewer terminal destinations (phagosomes) for EEs to fuse with, they may accumulate more extensively in the mutant than in their WT counterparts. An alternative is that within *bcd1* mutant cells, EEs are unable to fuse with their destination compartments. The apparent overlabeling of the few phagosomes present in the mutant population would again argue against this interpretation.

In summary, *bcd1* mutants exhibit a reduction of both pinocytosis and phagocytosis. We hypothesize that in the mutant, with a diminished set of terminal destinations (the phagosomes), EEs accumulate in the cytoplasm.

Recycling endosomes and secretory granules. *bcd1mutants show fewer, modestly larger "recycling" endosomes labeled with Cda12:mCherr, and an overabundance of secretory granules docked at the cell surface, with a newly observed association between them.*

In 2009, the Cole lab identified a novel gene (*CDA12*) whose product was localized to highly mobile, lozenge-shaped vesicles that frequently docked as punctae along ciliary rows (Zweifel *et al.*, 2009). FM labeling revealed that these were not pinosomes, though a FM probe eventually colocalized with the Cda12 product in larger, membrane-bound compartments. A CDA12 knockdown produced a fission-arrest phenotype. The combined localization data and the loss-of-function phenotype led the authors to hypothesize that Cda12p decorates the recycling endosome. Recycling endosomes (REs) in other organisms resemble our Cda12-decorated tubulovesicular compartments and have been shown to deliver membrane necessary for ingression of the fission zone during cytokinesis in animal models (Albertson *et al.*, 2005; Wilson *et al.*, 2005).

We generated both WT and *bcd1.2* mutants expressing the inducible, fluorescent Cda12:mCherry fusion product. This fusion gene (like others used in this study) is expressed when cells are exposed to $CdCl_2$ due to a metallothionein-inducible promoter cloned upstream from the ORF (Shang *et al.*, 2002). Cells were imaged at

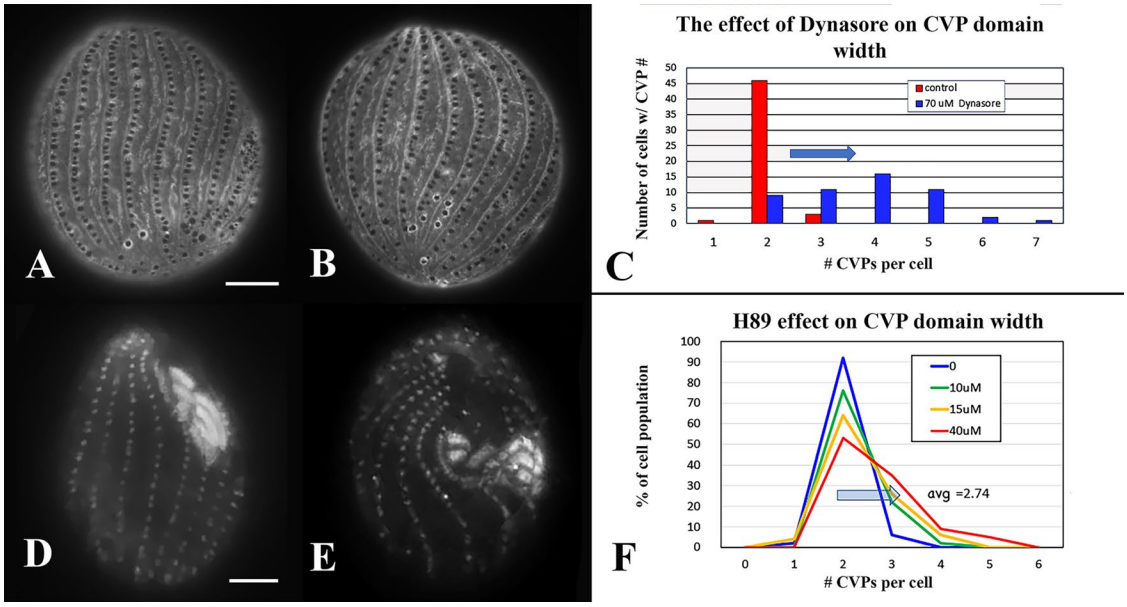

FIGURE 10: Effects of dynasore and H89 on CVP domain width in *Tetrahymena*. (A, B) Cells labeled with Tcb1:YFP. (A) WT control cell showing a typical pair of CVPs. (B) WT cell treated overnight with 70 µM dynasore, showing seven CVPs (an extreme phenocopy). (C) Plot showing CVP number in a population of WT cells grown with and without 70 µM dynasore (mean = 3.78 vs. 2.02 CVPs per cell, respectively, *N* = 100). (D, E) Two rare examples of cells treated with 40 µM PKA-inhibitor H89 overnight showing broadened OA. (Cells labeled with antibody to centrin.) Note that these two images were created by taking multiple focal plane images using conventional fluorescence microscopy (a Z-series) projected into a single image. (F) CVP domain broadening in cells with and without H89 treatment (*N* = 100).

various times following cadmium induction (early: 3–4 h and late: 12–18 h). Following early, 3–4 h, induction, *bcd1.1* cells exhibited fewer but modestly larger Cda12:mCherry-labeled compartments than were seen in WT cells (Figure 9, A–C). In one experiment (*N* = 50 for each genotype), *bcd1* cells exhibited a mean of 82.7 Cda12-labeled endosomes per cell (std = 23.9) with an average diameter of 1.3 µm in early expression (std = 0.14). WT control cells exhibited twice that number (144.3, std = 56.9) with an average diameter of 1.1 µm (std = 0.12). *T* tests run on both the number of endosomes and the endosome dimensions suggest that these means are significantly different ($P < 0.0001$). Most of these early-expression, CDA12-labeled endosomes were located deep within the cytoplasm (Figure 9, A and B).

Following a longer, 12–18 h, induction, Cda12:M-Cherry–decorated vesicles appeared to be docked in longitudinal rows at the cell cortex in both mutant and WT cells (Figure 9, D–G). We suspected that these later compartments were dense-core secretory granules or mucocysts. To test this, we coexpressed the red Cda12:mCherry with a green GFP-tagged Grl1 protein, one of the constituent proteins specific to mucocysts (Chilcoat *et al.*, 1996; Haddad *et al.*, 2002; Cowan *et al.*, 2005). Following a 3–6 h induction, we saw green, Grl1-containing vesicles in the deep cytoplasm, not yet docked at the cell cortex (Figure 9H, arrows). Red Cda12 labeling did not colocalize over these nascent, developing secretory granules (Figure 9I, bracket). Following 12–18 h induction, we saw clear colocalization over docked, mature mucocysts. In summary, *bcd1* mutant cells exhibit a significant reduction of Cda12-labeled compartments (candidates for recycling endosomes). Early after induced expression, the Cda12 label appears only over vesicles that are distinct from the developing secretory granules. Later, Cda12:mCherry shows a conspicuous colocalization with docked, mature secretory vesicles. Cda12:mCherry seems to localize strictly over mature, docked secretory vesicles. These results are consistent with reports that dense-core secretory granules (lysosome-related organelles, or LROs) fuse with early or recycling endosomes as a final step toward their maturation and docking (Delevoye *et al.*, 2009; Takahashi *et al.*, 2012; Marks *et al.*, 2013; Ma *et al.*, 2020).

Linking membrane traffic to cortical organelle broadening via PKA-regulated endocytosis. *Creating bcd1 phenocopies with H89 and dynasore.*

The *bcd1* mutant exhibits a highly pleiotropic phenotype. Two of the more conspicuous membrane-trafficking defects involve pinocytosis from parasomal sacs located at the base of each somatic cilium and phagocytosis associated with the complex OAs. Dynamin has been linked to both processes in *Tetrahymena*. Elde *et al.* (2005), investigating two of the eight *Tetrahymena* dynamin-related proteins, found one (Drp1) that was associated with parasomal sacs and the process of clathrin-mediated pinocytosis. *DRP1* knockout cells exhibited suppression of pinocytosis (Elde *et al.*, 2005). Elde *et al.* also observed Drp1 localization at the OA and deep fibers associated with phagocytosis, and cells expressing a predicted dominant-negative allele (K51E) showed a severe block in phagocytosis (A.P. Turkewitz, personal communication).

In mammalian systems, the GTPase inhibitor dynasore has been shown to inhibit dynamin-dependent endocytic events (Macia *et al.*, 2006). Dynasore also exhibits biological activity in ciliates. In *Paramecium bursaria*, a symbiotic algae, *Chlorella* survives ingestion by phagocytosis only if it can bud off from the initial digestive vacuole (the phagosome). This process can be imitated by feeding the cells microbeads of an appropriate size (Kodama and Fujishima, 2012). When *P. bursaria* are fed *Chlorella* in the presence of dynasore (40 µM), the authors observed *Paramecium* with a single, enlarged digestive vacuole filled with *Chlorella*. This demonstrates that dynasore has a pharmacological effect on endosome formation in ciliates, (in particular, during phagocytosis). A role for dynamin during

Paramecium phagocytosis was further demonstrated by Wiejak *et al.* (2003).

Learning that dynamin (Drp1) is necessary for both phagocytosis and pinocytosis in *Tetrahymena* (two processes also impacted by the *bcd1* mutation) and that the dynamin-GTPase inhibitor dynasore effectively interferes with phagocytosis in a related ciliate, we were curious to explore its effects on endocytosis in *Tetrahymena* and any (unlikely) impact that this might have on cortical organelle assembly. We treated WT cells with dynasore, examining both endocytosis and cortical organelle assembly. Growing WT (control cells) overnight in 70 µM dynasore resulted in cells with suppressed pinocytosis (Figure 7B), and with broadened CVP domains (Figure 10, A–C; mean = 3.78 vs. 2.02 CVPs per cell in one experiment; *T* test showed significance $P < 0.0001$).

Beige/BEACH-domain containing proteins NBEA in humans and *Rugose* in flies (Wang *et al.*, 2000, 2001) possess AKAP domains. PKA activity has been shown to promote endocytosis in multiple systems (Lukacs *et al.*, 1997; Hu *et al.*, 2001; Gururaj *et al.*, 2017) including *Paramecium* (Wiejak *et al.*, 2007). H89 inhibition of PKA has been shown to repress clathrin-mediated endocytosis (CME) (Kim *et al.*, 2005). In ciliates, H89 has been demonstrated to be effective at repressing PKA-dependent cellular activities such as regulating calcium-ATPase in *Paramecium* (Ray, 2008) and cyst induction in *Colpoda* (Sogame and Asami, 2011).

As demonstrated in our study, the Bcd1 protein localizes over sites of active pinocytosis and appears to be necessary for this process. Furthermore, it belongs to a gene family that exhibits PKA-anchor activities. Though the BCD1 AKAP-domain homology appears weak at best, it is not uncommon for ciliate genes to exhibit widely divergent predicted protein sequences while retaining homologous functions (Guerrier *et al.*, 2017). On the basis of these observations, we chose to explore the effects of H89, a known PKA inhibitor, on organelle domain broadening (Figure 10). Treating cells with 40 µM broad-spectrum, PKA-inhibitor H89 resulted in significant (though less extreme than the mutant) broadening of the CVP domain (Figure 10F; mean = 2.74 CVPs per cell vs. 2.02 in control cells). We also found rare examples of cells with broadened OAs among cells treated with H89. It should be noted that H89 also reduced cell division, meaning that some portion of the cell population was unable to divide while under the drug's influence. To observe the broadened-domain phenotype, cells must be able to divide and assemble the daughter cells' organelles under the restrictive conditions for the organelle phenotype to manifest. Nondividing cells will retain their original (WT) CVP and OA counts. Hence the H89 phenocopy likely underrepresents the effect.

DISCUSSION

We identified a gene, *BCD1*, in the ciliate *T. thermophila* that encodes a Beige/BEACH domain–containing protein similar to PKA-anchor proteins or AKAPs in other systems (Wang *et al.*, 2000). When the *Tetrahymena* gene is disabled by point mutation or deletion, the result is a highly pleiotropic phenotype affecting a wide variety of membrane-trafficking steps and the assembly of cortical, cytoskeleton-rich organelles. The Bcd1 protein localizes to ciliary pockets active in endocytosis, the OA active in phagocytosis, basal bodies, and cytoplasmic vesicles.

The *bcd1* loss-of-function phenotype involves "broadening of cortical domains" (Cole *et al.*, 1987). Preceding each cell division, ciliates assemble new cortical organelles so that each daughter cell is fully equipped to feed, excrete, and expel water. Where typically the subequatorial region of a single row of ciliated basal bodies becomes involved in basal body proliferation producing a new OP, *bcd1* mutants can recruit two or more neighboring ciliary rows to initiate basal body proliferation and oral assembly, resulting in supernumerary OPs. We suggest that during oral development, "cortical domains" are licensed to initiate basal body proliferation within the subequatorial region of a specific, ventral ciliary row. In the mutant, this cortical domain is broadened to license neighboring ciliary rows as well. During predivision development, WT cells specify another pair of ciliary rows in a supraequatorial region and to the cell's right of the stomatogenic kinety to nucleate assembly of the CVPs. In the *bcd1* mutant, we see the CVP-assembly domain spanning four or more ciliary rows. Mutant cells also exhibit broadening of the cortical domain within which Cyps are assembled.

In the present study we learned that *bcd1* loss-of-function mutations also affect numerous processes involved in membrane trafficking in the ciliate *Tetrahymena*. Loss-of-function mutations in Beige/BEACH domain genes within other organisms are linked to endosome fission/fusion defects and to lysosome enlargement (Durchfort *et al.*, 2012; Cullinane *et al.*, 2013). *bcd1* mutants show reduced uptake of fluorescent FM probe via pinocytosis. Paradoxically, *bcd1* mutants exhibit an overabundance of EEs (poorly labeled with the FM-43 probe due to suppression of pinocytosis, but richly labeled with the Rab22:GFP marker). We interpret these results to mean that EEs are still being produced in the mutant cell (likely from *trans*-Golgi–derived membrane), though they are no longer richly supplemented through pinocytosis. We observed a similar overabundance of LEs/lysosomes labeled with Rab7:YFP.

bcd1 mutants also exhibit a dramatic suppression of feeding through phagosome production. The phagosomes that do form in the *bcd1* mutant exhibit excess labeling, with markers delivered from both early and late endosomes, and these phagosomes appear to have difficulty with terminal egestion, suggesting either diminished phagosome fusion at the Cyp or increased phagosome tethering.

Reduced phagocytosis in the *bcd1* mutants has an uncertain etiology. The *bcd1* phenotype involves assembly of multiple, side-by-side oral primordia. After the initial proliferation of basal bodies, the supernumerary membranelles integrate into enlarged, occasionally misshapen mature mouths (Cole *et al.*, 1987). It should also be noted that 15–20% of the *bcd1* mutant population may be undergoing ORP, an alternative developmental pathway triggered in WT cells that have been subjected to amino acid deprivation (Nelsen and DeBault, 1978; Nelsen, 1981). Cells undergoing ORP would also be removed from the feeding population. That said, ORP would account for, at most, only a 20% reduction in the feeding population within *bcd1* mutants, while the actual nonfeeding subpopulation is closer to 80%. If phagocytosis is not suppressed due to structural issues related to oral assembly in the mutant, that directs attention to the membrane dynamics associated with phagocytosis itself. Phagosome formation requires membrane delivery as "discoidal vesicles" swarm and fuse with the nascent vacuole (Nilsson, 1987; Baumert *et al.*, 1998). Phagosome maturation involves subsequent membrane removal as well, as phagosomes "dehydrate" and shrink (Nilsson, 1987). It is an open question whether *bcd1* mutant OAs are mechanically impaired and consequently inefficient at collecting food particles or whether the *bcd1* mutants exhibit diminished food vacuole formation as a consequence of vesicle fission/fusion defects.

Whatever its cause, the reduction in food vacuole formation appears to trigger a suite of downstream consequences involving what we have termed "destination failure," a form of intracellular pleiotropy. In starved WT cells, cationized ferritin enters *Tetrahymena* cells through parasomal sacs located at the base of every cilium, and the resulting labeled EEs find their way to the phagosomes

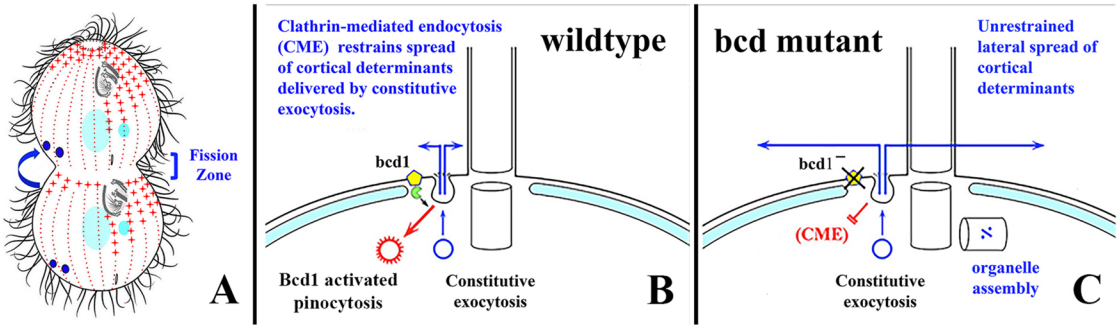

FIGURE 11: (A) Diagram of a dividing WT cell with Bcd1 depicted in red (foci located in ciliary pockets near basal bodies, sites of active membrane exchange). Bcd1p appears more concentrated at the anterior end of the cell, though during cell division it can be seen throughout. (B) Model of WT cortical dynamics as we envision them, with a balance between delivery of organelle assembly components/determinants via constitutive exocytosis (blue) and retrieval of excess material via CME (red). Bcd1 (yellow) is a cortical protein, possibly serving as a kinase anchor that stimulates localized endocytosis. The potential PKA-anchor function of this particular Beige/BEACH domain containing protein remains somewhat tenuous. (C) In *bcd1* mutants, delivery of cortical organelle components/determinants continues unabated, but without the cortical foci of Bcd1 activity, endocytosis is reduced, causing a net excess in delivery of organelle assembly determinants and broadening of organelle assembly platforms, depicted here as a field of basal body proliferation.

(Nilsson and Van Deurs, 1983). In WT cells, we observed FM- and Rab22-labeled EEs as well as Rab7-labeled LEs associating with food vacuoles, and these phagosomes quickly took on the endosome probes' fluorescence characteristics. We propose that in cells with reduced numbers of phagosomes, there are fewer destinations for both early and late endosome trafficking. Without this terminal destination, these smaller endosomal compartments accumulate in the cytoplasm. Alternatively, WT Bcd1 function might be necessary for both early and late endosome fusion to the phagosomes (or there could be a combination of both destination failure and fusion failure). The elevated brightness of Rab7 labeling (LEs/lysosomes) and Rab22 labeling (EEs) over the sparse *bcd1* mutant phagosomes argues that endosome fusion function is still intact in the mutant but with fewer target destinations; we may actually be seeing elevated endosome fusion in the phagosomes that are successfully created.

It may be profitable to look to cortical organelle assembly processes in metazoan models for insights linking endosome trafficking to dimensional control of cortical organelles. *Drosophila* offers two interesting examples: adherens junctions that form between epithelial cells of the imaginal discs (Woolworth *et al.*, 2009) and synaptic boutons that form at the neuromuscular junction (Dickman *et al.*, 2006). In the former, the *Drosophila awd* mutants (abnormal wing disc) result in down-regulation of Rab5-mediated endocytosis. With diminished endocytosis, researchers observed accumulation and spread of adherens junction components such as E-cadherin, β-catenin/Armadillo, and α-spectrin resulting in enlarged adherens junctions (a broadened cortical domain). In the case of neural development, a whole variety of mutants with endocytosis defects have been shown to form supernumerary synaptic boutons: axon termini specialized for exocytic, neurotransmitter secretion. In both examples, endocytosis has been implicated in regulating the dimensions and numbers of cortical organelles, with down-regulation of endocytosis leading to expansion of the cortical organelles involved.

In light of these examples and the evidence we have collected, we conjectured that in *Tetrahymena*, organelle assembly platforms, once targeted to their appropriate cortical locations, require a balance between the delivery of organelle assembly components though constitutive exocytosis and retrieval of excess assembly components through endocytosis. We predicted that pharmacological suppression of dynamin-mediated pinocytosis should suppress the retrieval pathway and result in excess delivery of organelle assembly components, with a consequent hypertrophy of cortical organelles in dividing WT cells. Treatment with 70 μM dynasore (a potent dynamin GTPase inhibitor) suppressed pinocytosis in *Tetrahymena* and showed a dramatic, repeatable broadening of the CVP domain. Our attempts to suppress PKA activity using commercial inhibitors was less convincing. We note that sequence homology between the *BCD1* and metazoan AKAP domains is weak. It could be that, while capturing several of the functional domains seen in RUGOSE (*Drosophila*) and NBEA (humans), the *Tetrahymena BCD1* gene may have a highly modified AKAP domain, and its ligand could be something other than PKA. Even conventional AKAP proteins can anchor a variety of protein ligands, including other kinases, phosphatases, elements of the actin cytoskeleton, and calcium-binding proteins, among others (Feliciello *et al.*, 2001). It has been suggested that AKAPs serve as signal "transduceosomes" mediating local protein phosphorylation events.

Though functional Bcd1 ligands remain unidentified, the ability to phenocopy CVP domain broadening by suppressing pinocytosis led us to propose a role for Bcd1 in stimulating CME from parasomal sacs located at the base of each somatic cilium. By stimulating endocytosis, the WT Bcd1 may promote retrieval of excess organelle-assembly components, balancing their delivery by some as-yet-uncharacterized exocytic delivery pathway. A diagram of Bcd1 distribution and the model we envision appears in Figure 11. Bcd1 appears in the right place and time to influence dimensions of the developing OP via basal body proliferation (Figure 11A, right arrow). When Bcd1 is absent as in the *bcd1* mutants, there is a resulting overdelivery of stomatogenic determinants, and OP assembly spreads into the cortex normally occupied by the Bcd1 gene product. This suggests a role in limiting the lateral spread of the organelle assembly process. We propose that Bcd1-anchored activity stimulates endocytosis from parasomal sacs located at the base of every cilium, thereby retrieving excess organelle assembly components or determinants (Figure 11B). In the *bcd1* mutants, this particular activity may be absent from the peri–basal body foci, where endocytosis is diminished. With constitutive delivery of organelle assembly components (or determinants) unimpaired and diminished retrieval of excess materials, there would be a net broadening of the organelle assembly platform (Figure 11C).

It is noteworthy that Beige/BEACH domain-containing proteins homologous to our pleiotropic ciliate pattern gene have roles in human disease, including Chediak–Higashi syndrome, a rare immune disorder (Sharma *et al.*, 2020), Fragile-X mental retardation (Sears *et al.*, 2019), Parkinson's disease, and autism (Wild and Dell'Acqua, 2018). In mouse LRBA mutants (a mammalian Beige/BEACH-domain–encoding gene), delivery of proteins necessary for assembly of stereocilia in the inner ear is affected, resulting in deafness (Vogl *et al.*, 2017). Humans possess a similar mutation. Given the dramatic, quantifiable aspects of our ciliate phenotype, this work potentially offers *Tetrahymena* as a model for exploring defects in Beige/BEACH domain protein activities and their potential role in cortical patterning and intracellular signal transduction.

Our work also highlights further questions related to pattern formation within single cells. What mechanisms determine anterior–posterior and circumferential locations of cortical organelles including the fission zone, OP, CVP, and Cyp? Significant progress has been made in identifying both genes and potential mechanisms behind anterior–posterior localization (see Cole and Gaertig, 2022, for a review). With A/P patterning, it appears that antagonistic, inhibitory gradients extend from both the anterior and posterior poles of the cell, restricting organelle assembly to the midbody cortical region in which both inhibitors exist in low concentrations. It may be significant that most of these A/P pattern gene products are localized in regions surrounding the basal bodies and many or most represent kinases or proteins that regulate kinase activities. We are compelled to recognize an increasingly significant role for the peri–basal body space and the ciliary pit as an arena for signals regulating cortical patterning. Regarding the ciliate's virtuosity for circumferential patterning, mutant searches have identified numerous promising pattern gene loci that may play a role (see Frankel, 2008, for a review). The circumferential pattern mutants identified in *Tetrahymena* include *bcd1*, *janA*, *janB*, *janC*, and *hpo* (hypoangular). This paper is the first to identify and characterize a circumferential pattern gene in ciliates.

MATERIALS AND METHODS

Request a protocol through *Bio-protocol*.

Tetrahymena strains and culture conditions

WT B2086.2 (RRID TSC_SD00709), SB1969 (RRID TSC_SD00701), and CU428.2 (RRID TSC_SD00178) strains of *T. thermophila* were provided by Donna Cassidy-Hanley at the Tetrahymena Stock Center, Cornell University. *bcd1* strains were from mutant stocks: IA342 (RRID TSC_ SD00635), (*bcd1-1/bcd1-1; eja1-1/eja1-1* [*bcd1-1; eja1-1*; bcd1, eja1, II]), IA344 (RRID TSC_SD006356) (*bcd1-1/bcd1-1; eja1-1/eja1-1* [*bcd1-1; eja1-1*; bcd1, eja1, VII]), IA378 (RRID TSC_ SD00641) (bcd1-2/bcd1-2 [bcd1-2*; bcd1, II*]), *and IA379* (RRID TSC_ SD00642) (bcd1-2/bcd1-2 [bcd1-2*; bcd1, V*]). Unless stated otherwise, cells were grown at 30°C in "NEFF" medium (0.25% proteose peptone, 0.25% dextrose, 0.5% yeast extract, 0.009% ferric EDTA).

Identification of the *bcd1-1* mutation

A mutant *T. thermophila* strain homozygous for *bcd1-1 and mpr1-1* (IA405- RRID TSC_SD00646) was outcrossed to CU427.4 (RRID TSC_SD00715) (a cycloheximide-resistant heterokaryon), and the double drug–resistant (6-methylpurine [6mp] and cycloheximide [cy]) F1 progeny clones were selected. Several F1s were propagated vegetatively, and cy-sensitive "macronuclear assortant" clones were identified by replica plating. To obtain clones homozygous for either *bcd1-1* or WT BCD1, we used the method of "two round genomic exclusion." A single cy-sensitive F1 was crossed to A*III and pairs were isolated and allowed to multiply in drops to high density. A total of resulting 168 "synclones" (containing mixed progeny derived from both sides of the F1 x A*III conjugation) were replicated onto wells containing starvation buffer (10 mM Tris-HCl, pH 7.5) and allowed to mate to undergo the second round of genomic exclusion. The F2 progeny was selected in the growth medium cy 15 mg/ml. A total of 62 cy-resistant F2 progeny was recovered and tested for the cortical phenotype using 20H5 anti-centrin (see below). Among them 32 and 30 progeny were determined to be WT and *bcd1-1*, respectively. The cy-resistant F2 UPC progeny were cloned and screened for the *bcd1-1* cortical phenotype by immunofluorescence using the anti-centrin monoclonal antibody 20H5. The WT and mutant F2 progeny were pooled, and the pools were grown to a mid–log phase and starved for 2 d at room temperature in 60 mM Tris-HCl, pH 7.5. Total genomic DNA was extracted using the urea method (Dave *et al.*, 2009). The pool DNAs were used to make genomic libraries using Illumina Truseq primer adapters and sequenced on an Illumina HiSeq X instrument, which generated paired-end reads of 150-base-pair length at 90× genome coverage. The MiModD suite of tools version 0.1.8 (https://sourceforge.net/projects/mimodd/) was used for ACCA-based variant mapping and identification (Jiang *et al.*, 2017) as follows. The sequencing reads were aligned to the micronuclear reference genome (GenBank assembly accession GCA_000261185.1; Hamilton *et al.*, 2016), and the aligned reads from both pools were used for joint multisample variant calling. The variant call data set was filtered for sites with high coverage for each of the two pools. Linkage scores contrasting the allelic composition of the mutant with that of the WT pool were computed for each variant and the results plotted against micronuclear genome coordinates. For variant identification, the same sequencing reads were aligned to the macronuclear reference genome (GenBank assembly accession GCA_000189635 [Eisen *et al.*, 2006]) and the aligned reads subjected to variant calling as above.

To create a null macronuclear allele for *TTHERM_ 00035550*, we used the "codeletion" method based on expression of scan RNAs that target the genome in the developing macronucleus for deletion (Hayashi and Mochizuki, 2015). An 872-base-pair fragment of *TTHERM_ 00035550* (located between positions 953 and 1824 base pairs of the predicted coding region) was cloned into the *Not*I site of the pMcodel rDNA vector using Gibson Assembly. The resulting pMcodel-BCD1 plasmid was introduced into mating B2086 and CU428 *Tetrahymena* cells (at ~8 h after mixing of the two strains at 30°C) using biolistic bombardment (Cassidy-Hanley *et al.*, 1997). Transformants were selected in Supplemented proteose peptone medium (SPP; 2% proteose peptone, 0.1% yeast extract, 0.2% glucose, 33 μM $FeCl_3$) with 100 mg/ml paromomycin. Four independent "codel" clones were isolated and all confirmed to contain deletions in the targeted region using primers with sequences located outside of the *Not*I insertion site, within the sequence of rDNA. We analyzed the co-del Δ2 strain.

Identification of the *bcd1-2* allele

Genomic DNA was isolated from *bcd1-2*, *T. thermophila* strains by disrupting the cells in ~10 volumes of nuclei lysis solution (Promega, Madison, WI) at 65°C for 30 min, followed by treatment with 30 μg of RNase A at 37°C for 15 min. Denatured protein and cell debris were removed by vigorous mixing with a one-third volume of protein precipitate solution (Promega, Madison, WI) followed by centrifugation for 3 min at 13,000 × *g*; subsequently DNA was recovered by isopropanol precipitation. Solubilized genomic DNA was used as template in PCR with various combinations of primers (listed in Supplemental Table 1) to amplify segments of the *BCD1* locus. Amplified products were sequenced (Genewiz, Chelmsford, MA)

using oligonucleotide primers internal to each product. To confirm that the identified A-G base change in the *bcd1-2* allele created a novel splice site, RNA was isolated from WT or *bcd1-2* strains using the RNAeasy Mini Kit (Qiagen, Germantown, MD) and the mRNA region spanning the mutation was amplified by reverse transcriptase PCR as previously described (Malone *et al.*, 2005). The amplified products were sequenced to determine the effect of the mutation on the *bcd1-2* mRNA.

Phagocytosis assay

Cells were grown to mid–log phase of the growth curve (200–300,000 cells per ml). We mixed 500 µl of *Tetrahymena* culture in a microfuge tube with 500 µl of 1% India ink and let sit at room temperature. At 5-min intervals, we took a 30 µl sample of *Tetrahymena* and ink and placed it on a microscope slide. We then quickly added 5 µl of a 5% glutaraldehyde solution to the 30 µl sample and mixed with the pipette tip. We then applied a coverslip and counted the vacuoles at 400× magnification view until 100 randomly chosen specimens were scored.

Pinocytosis assay

Cells were grown to mid–log phase conditions (200–300,000 cells/ml), pelleted, and washed in 10 mM Tris buffer (pH 10.4). Cells were labeled and examined either 3 or 18 h after starvation (Elde *et al.*, 2005). Cells (1 ml) were placed in an Eppendorf tube and 1 µl of 5 mM FM 1-43 (Molecular Probes, Eugene, OR) delivered and timed. At 5-min intervals, 11 µl of labeled cells was placed on a slide with a 22 mm square coverslip. Alternatively, cells were immobilized using the Ringlein differential screw cell compressor (Cole *et al.*, 2002). Cells were imaged using an Olympus BX50 fluorescence microscope and a C-Mos digital camera. To assess comparative FM-probe uptake, the camera exposure times were kept constant. To observe the relatively faint-staining *bcd1* endosome uptake, the concentration of FM probe was doubled and exposure times increased.

Imaging Crn1:YFP-labeled compartments

This construct required special handling for consistent imaging. Free-swimming cells had very few Crn1:YFP-labeled "terminal vacuoles" docked at the Cyp (10–15% of cells). As the coverslip made contact and began to immobilize the labeled cells, an increasing number of them revealed Crn1-decorated vacuoles at the Cyp. With more time spent immobilized beneath the coverslip, Crn1:YFP-labeled phagosomes began to accumulate even in the WT controls. We suspect that physical compression by slide/coverslip inhibits vacuole egestion, causing a "back-up" of Crn12:YFP-labeled phagosomes, unable to egest. To collect accurate data from Crn1:YFP-labeled specimens, these were first fixed in 2% paraformaldehyde, washed in PHEM buffer (60mM PIPES, 25mM HEPES, 10mM EGTA, 2mM $MgCl_2$, pH 6.9), and then observed. Following this procedure, labeled phagosome counts remained consistent.

Immunofluorescence-based imaging of Bcd1

To study the localization pattern of the Bcd1 protein under conditions of expression that are close to native, we attached a sequence encoding GFP to the 3′ end of the coding region of native TTHERM_00637770 with a linked pur (puromycin resistance) selectable marker gene (Iwamoto *et al.*, 2014) by gene replacement. To construct the needed targeting plasmid, the homology arms were amplified from portions of the *TTHERM_00637770*/BCD1 coding region (primers 5′-AAATACGCGTGGTACAACAATCCAGTTCAT CAAG-3′ and 5′ AATTGGATC CCTTCTACTATTCATTATTATTTGAATTAGATCTACCTAG-3′) and its 3′UTR (primers 5′-AATTCTCGAGAAGCTTATTTAATTTTAAATGTGTGAGGAGG-3′ and 5′-AAATCTGCAGTGATGTTTCTTAAACTAAGCCTTCTC-3′) used to replace the corresponding fragments of *RSP4* on the plasmid pRSP4/6A-pPur (Joachimiak *et al.*, 2021). The resulting plasmid pBCD-GFP-Pur was digested with *Mlu*I and *Xho*I and introduced into starved CU428 *Tetrahymena* cells using biolistic bombardment, and transformants were selected in the growth medium with puromycin 200 µg/ml. The transgene copy number was increased through phenotypic assortment, by growing transformant clones at increasing concentrations of paromomycin.

Assorted clones were analyzed by immunofluorescent polyclonal anti-GFP (Rockland) antibodies (1:800 dilution), followed by secondary antibodies labeled with CY3 (Rockland); DNA was stained with DAPI (4′,6-diamidino-2-phenylindole). The images were collected on a Zeiss LSM 880 confocal microscope. Super-resolution structured illumination microscopy (SR-SIM) imaging was conducted on an ELYRA S1 microscope equipped with a 63× NA 1.4 Oil Plan-Apochromat differential interference contrast microscopy (DIC) objective. The Z stack slices were analyzed by Fiji/ImageJ (Z project tool).

Immunofluorescence imaging of various subcellular compartments

Cells were fixed and stained with antibodies as described by Jiang *et al.* (2020). Samples were air-dried at 30°C, and the cover glass was washed three times with phosphate-buffered saline (PBS) and incubated with primary antibodies diluted in PBS supplemented with 3% bovine serum albumin fraction V and 0.01% Tween-20. The primary antibodies used were polyclonal anti-GFP (Rockland; 1:800 dilution), monoclonal anti-centrin 20H5 (EMD Millipore; 1:400; Salisbury *et al.*, 1988), and monoclonal anti-fenestrin (3A7) (Nelsen *et al.*, 1994). The secondary antibodies were conjugated to either TRITC or FITC (Rockland; 1:300). The nuclei were costained with DAPI (Sigma-Aldrich). The labeled cells were embedded in VectaShield antiquenching mounting medium for fluorescence (VectorLabs)

Tagging *Tetrahymena* genes with fluorescent protein tags for imaging of subcellular compartments

T. thermophila strains that expressed fluorescent protein–tagged proteins were created by introducing linearize expression constructs that integrate into either the *BTU1* or *RPL29* locus upon biolistic transformation (Cassidy-Hanley *et al.*, 1997). To control expression, each protein, tagged on either its amino (N)- or carboxy (C)-terminus, was present downstream of the cadmium-inducible *MTT1* promoter (Shang *et al.*, 2002). Gateway recombination cloning was used to generate expression plasmids (Supplemental Table 2). First, the desired coding regions of each gene of interest were amplified from *Tetrahymena* genomic DNA by using coding region–specific primers (Supplemental Table 3) and Phusion DNA polymerase in PCRs (New England Biolabs, Ipswich, NY) followed by cloning of the amplified products into the pENTR-D entry vector by topoisomerase-mediated cloning (Invitrogen/Life Technologies, Carlsbad, CA). Oligonucleotide primers were designed, with assistance of the Primer3 Program (http://frodo.wi.mit.edu/), to amplify the entire coding regions starting six bases upstream of the predicted ATG start codon and ending with the last codon, excluding the stop codon when tagging on the coding region on the C-terminus was planned. The sequence CACC was added to the 5′ end of the upstream primer to facilitate directional cloning into pENTR/D, and GATATC (an *Eco*RV site) or GGATCC (a *Bam*HI site) was added to the 5′ end of the downstream primer to confirm cloning of the full-length product. Each integrative expression vector contained a Gateway recombination cassette (Invitrogen/Life Technologies), allowing LR Clonase II to catalyze the exchange of the coding region

in entry vector pENTR to place it downstream of the *MTT1* promoter and in frame with a specific fluorescent protein (see Supplemental Table 3). The expression plasmids that integrate upstream of the *RPL29* locus contain a cycloheximide-resistant allele of the rpL29 gene to direct its integration and allow for selection of transformants in 1× SPP medium containing 12.5 µg/ml cycloheximide. Expression plasmids that integrate into the *BTU1* locus were created by modifying the Cas9 expression vector pC9T (created by K. Mochizuki and obtained from the Tetrahymena Stock Center; TSC_ PID00038). Transformants were selected in 1× SPP medium containing 100 µg/ml paromomycin. Transgene expression was induced by the addition of 0.3–1 µg/ml $CdCl_2$, and cells were grown 2–20 h before protein accumulation was monitored.

Drug treatment

Dynasore (obtained from Millipore/Sigma) was dissolved in dimethyl sulfoxide (DMSO) (stock solution = 12.5 mg/ml) and diluted to a final concentration of 70 µM for live cell cultures. H89 (obtained from Millipore/Sigma) was dissolved in DMSO, and various concentrations tested for maximum CVP domain broadening. We found that a 40 µM concentration produced the most severe CVP domain broadening. It should be noted that researchers have reported off-target effects for both of these drugs (see Murray, 2008; Preta *et al.*, 2015).

ACKNOWLEDGMENTS

Research in the Cole/Chalker laboratories was supported by National Science Foundation Grant no. 1947608. Research in the Gaertig lab was supported by National Institutes of Health Grant no. 5R01GM135444. Significant data collection was conducted by St. Olaf undergraduates: Benjamin Reister, Kavya Guntabonu, and Kara Gerads.

REFERENCES

Albertson R, Riggs B, Sullivan W (2005). Membrane traffic: a driving force in cytokinesis. Trends Cell Biol 15, 92–101.

Allen RD (1967). Fine structure reconstruction, and possible functions of components of the cortex of *Tetrahymena pyriformis*. J Protozool 14, 553–565.

Allen RD (1984). Paramecium Phagosome Membrane: From Oral Region to Cytoproct and Back Again 1. J Protozool 31, 1–6.

Allen RD, Fok AK (1993). Endosomal membrane traffic of ciliates. Adv Cell Mol Biol Membr 2B, 283–309.

Baumert U, Vosskuhler C, Tiedtke A (1998). Formation and maturation of phagosomes labeled by magnetic micro particles: an ultrastructural study in *Tetrahymena thermophila*. Eur J Protistol 34, 291–300.

Benz PM, Ding Y, Stingl H, Loot AE, Zink J, Wittig I, Popp R, Fleming I (2020). AKAP12 deficiency impairs VEGF-induced endothelial cell migration and sprouting. Acta Physiol (Oxf) 228, e13325.

Bright LJ, Kambesis N, Nelson SB, Jeong B, Turkewitz AP (2010). Comprehensive analysis reveals dynamic and evolutionary plasticity of Rab GTPases and membrane traffic in *Tetrahymena thermophila*. PLoS Genet 6, e1001155.

Bruns PJ, Brussard TB, Merriam EV (1983). Nullisomic *Tetrahymena:* a set of nullisomics define the germinal chromosomes. Genetics 104, 257–270.

Burgess A, Mornon JP, de Saint-Basile G, Callebaut I (2009). A concanavalin A-like lectin domain in the CHS1/LYST protein, shared by members of the BEACH family. Bioinformatics 25, 1219–1222.

Cassidy-Hanley D, Bowen J, Lee JH, Cole E, VerPlank LA, Gaertig J, Gorovsky MA, Bruns PJ (1997). Germline and somatic transformation of mating *Tetrahymena thermophila* by particle bombardment. Genetics 146, 135–147.

Chilcoat ND, Melia SM, Haddad A, Turkewitz AP (1996). Granule lattice protein 1 (Grl1p), an acidic, calcium-binding protein in Tetrahymena thermophila dense-core secretory granules, influences granule size, shape, content organization, and release but not protein sorting or condensation. J Cell Biol 135, 1775–1787.

Cole E, Gaertig J (2022). Anterior-posterior pattern formation in ciliates. J Eukaryot Microbiol 69, e12890.

Cole ES, Anderson PC, Fulton RB, Majerus ME, Rooney MG, Savage JM, Chalker D, Honts J, Welch ME, Wentland AL, *et al.* (2008). A proteomics approach to cloning fenestrin from the nuclear exchange junction of *Tetrahymena*. J Eukaryot Microbiol 55, 245–256.

Cole ES, Frankel J, Jenkins LM (1987). *bcd:* a mutation affecting the width of organelle domains in the cortex of *Tetrahymena thermophila*. Wilhelm Roux's Arch Dev Biol 196, 421–433.

Cole ES, Stuart KR, Marsh TC, Aufderheide K, Ringlien W (2002). Confocal fluorescence microscopy for *Tetrahymena thermophila*. In: Cell Biological Applications of Confocal Microscopy, ed. B. Matsumoto, 2nd ed., 338–360.

Cowan AT, Bowman GR, Edwards KF, Emerson JJ, Turkewitz AP (2005). Genetic, genomic, and functional analysis of the granule lattice proteins in Tetrahymena secretory granules. Mol Biol Cell 16, 4046–4060.

Cullinane AR, Schaffer AA, Huizing M (2013). The BEACH is hot: a LYST of emerging roles for BEACH-domain containing proteins in human disease. Traffic 14, 749–766.

Dave D, Wloga D, Gaertig J (2009). Manipulating ciliary protein-encoding genes in Tetrahymena thermophila. Methods Cell Biol 93, 1–20.

Delevoye C, Hurbain I, Tenza D, Sibarita JB, Uzan-Gafsou S, Ohno H, Geerts WJ, Verkleij AJ, Salamero J, Marks MS, Raposo G (2009). AP-1 and KIF13A coordinate endosomal sorting and positioning during melanosome biogenesis. J Cell Biol 187, 247–264.

Dickman DK, Lu Z, Meinertzhagen IA, Schwarz TL (2006). Altered synaptic development and active zone spacing in endocytosis mutants. Curr Biol 16, 591–598.

Durchfort N, Verhoef S, Vaughn MB, Shrestha R, Adam D, Kaplan J, Ward DM (2012). The enlarged lysosomes in beige j cells result from decreased lysosome fission and not increased lysosome fusion. Traffic 13, 108–119.

Eisen JA, Coyne RS, Wu M, Wu D, Thiagarajan M, Wortman JR, Badger JH, Ren Q, Amedeo P, Jones KM, *et al.* (2006). Macronuclear genome sequence of the ciliate *Tetrahymena thermophila*, a model eukaryote. PLoS Biol 4, e286.

Elde NC, Morgan G, Winey M, Sperling L, Turkewitz AP (2005). Elucidation of clathrin-mediated endocytosis in tetrahymena reveals an evolutionarily convergent recruitment of dynamin. PLoS Genet 1, e52.

Feliciello A, Gottesman ME, Avvedimento EV (2001). The biological functions of A-kinase anchor proteins. J Mol Biol 308, 99–114.

Frankel J (1969). Participation of the undulating membrane in the formation of oral replacement primordia in *Tetrahymena pyriformis*. J Protozool 16, 26–35.

Frankel J (2008). What do genic mutations tell us about the structural patterning of a complex single-celled organism? Eukaryot Cell 7, 1617–1639.

Frankel J, Heckmann K (1968). A simplified Chatton-Lwoff silver impregnation procedure for use in experimental studies with ciliates. Trans Am Microsc Soc 87, 317–321.

Guerrier S, Plattner H, Richardson E, Dacks JB, Turkewitz AP (2017). An evolutionary balance: conservation vs innovation in ciliate membrane trafficking. Traffic 18, 18–28.

Gururaj S, Evely KM, Pryce KD, Li J, Qu J, Bhattacharjee A (2017). Protein kinase A–induced internalization of Slack channels from the neuronal membrane occurs by adaptor protein-2/clathrin–mediated endocytosis. J Biol Chem 292, 19304–19314.

Haddad A, Bowman GR, Turkewitz AP (2002). New class of cargo protein in Tetrahymena thermophila dense core secretory granules. Eukaryot Cell 1, 583–593.

Hamilton EP, Kapusta A, Huvos PE, Bidwell SL, Zafar N, Tang H, Hadjithomas M, Krishnakumar V, Badger JH, Caler EV, *et al.* (2016). Structure of the germline genome of *Tetrahymena thermophila* and relationship to the massively rearranged somatic genome. eLife 5, e19090.

Han JD, Baker NE, Rubin CS (1997). Molecular characterization of a novel A kinase anchor protein from Drosophila melanogaster. J Biol Chem 272, 26611–26619.

Hayashi A, Mochizuki K (2015). Targeted gene disruption by ectopic induction of DNA elimination in Tetrahymena. Genetics 201, 55–64.

Hirono M, Nakamura M, Tsunemoto M, Yasuda T, Ohba H, Numata O, Watanabe Y (1987). Tetrahymena actin: localization and possible biological roles of actin in Tetrahymena cells. J Biochem 102, 537–545.

Hohenester E, Tisi D, Talts JF, Timpl R (1999). The crystal structure of a laminin G–like module reveals the molecular basis of α-dystroglycan binding to laminins, perlecan, and agrin. Mol Cell 4, 783–792.

Hu MC, Fan L, Crowder LA, Karim-Jimenez Z, Murer H, Moe OW (2001). Dopamine acutely stimulates Na+/H+ exchanger (NHE3) endocytosis via clathrin-coated vesicles: dependence on protein kinase A-mediated NHE3 phosphorylation. J Biol Chem 276, 26906–26915.
Iwamoto M, Mori C, Hiraoka Y, Haraguchi T (2014). Puromycin resistance gene as an effective selection marker for ciliate Tetrahymena. Gene 534, 249–255.
Jiang YY, Maier W, Baumeister R, Minevich G, Joachimiak E, Ruan Z, Kannan N, Clarke D, Frankel J, Gaertig J (2017). The Hippo pathway maintains the equatorial division plane in the ciliate Tetrahymena. Genetics 206, 873–888.
Jiang YY, Maier W, Chukka UN, Choromanski M, Lee C, Joachimiak E, Wloga D, Yeung W, Kannan N, Frankel J, Gaertig J (2020). Mutual antagonism between Hippo signaling and cyclin E drives intracellular pattern formation. J Cell Biol 219, e202002077.
Joachimiak E, Osinka A, Farahat H, Swiderska B, Sitkiewicz E, Poprzeczko M, Fabczak H, Wloga D (2021). Composition and function of the C1b/C1f region in the ciliary central apparatus. Sci Rep 11, 11760.
Kelley LA, Mezulis S, Yates CM, Wass MN, Sternberg MJ (2015). The Phyre2 web portal for protein modeling, prediction and analysis. Nat Protoc 10, 845–858.
Kim SJ, Choi WS, Han JSM, Warnock G, Fedida D, McIntosh CH (2005). A novel mechanism for the suppression of a voltage-gated potassium channel by glucose-dependent insulinotropic polypeptide: protein kinase A-dependent endocytosis. J Biol Chem 280, 28692–28700.
Kodama Y, Fujishima M (2012). Characteristics of the digestive vacuole membrane of the alga-bearing ciliate Paramecium bursaria. Protist 163, 658–670.
Letunic I, Doerks T, Bork P (2015). SMART: recent updates, new developments and status in 2015. Nucleic Acids Res 43(Database issue), D257–D260.
Lukacs LG, Segal G, Kartner N, Grinstein S, Zhang F (1997). Constitutive internalization of cystic fibrosis transmembrane conductance regulator occurs via clathrin-dependent endocytosis and is regulated by protein phosphorylation. Biochem J 328, 353–361.
Ma CIJ, Yang Y, Kim T, Chen CH, Polevoy G, Vissa M, Burgess J, Brill JA (2020). An early endosome–derived retrograde trafficking pathway promotes secretory granule maturation. J Cell Biol 219, e201808017.
Macia E, Ehrlich M, Massol R, Boucrot E, Brunner C, Kirchhausen T (2006). Dynasore, a cell-permeable inhibitor of dynamin. Dev Cell 10, 839–850.
Malone CD, Anderson AM, Motl JA, Rexer CH, Chalker DL (2005). Germ line transcripts are processed by a Dicer-like protein that is essential for developmentally programmed genome rearrangements of *Tetrahymena thermophila*. Mol Cell Biol 25, 9151–9164.
Marks MS, Heijnen HF, Raposo G (2013). Lysosome-related organelles: unusual compartments become mainstream. Curr Opin Cell Biol 25, 495–505.
Masuyer G, Conrad J, Stenmark P (2017). The structure of the tetanus toxin reveals pH-mediated domain dynamics. EMBO Rep 18, 1306–1317.
Murray AJ (2008). Pharmacological PKA inhibition: all may not be what it seems. Sci Signal 1, re4.
Nelsen EM (1978). Transformation in *Tetrahymena pyriformis:* development of an inducible phenotype. Dev Biol 66, 17–31.
Nelsen EM (1981). The undulating membrane of *Tetrahymena:* formation and reconstruction. Trans Am Microsc Soc 100, 285–295.
Nelsen EM, DeBault LE (1978). Transformation in *Tetrahymena pyriformis*—description of an inducible phenotype. J Protozool 25, 113–119.
Nelsen EM, Williams NE, Yi H, Knaak J, Frankel J (1994). "Fenestrin" and conjugation in *Tetrahymena thermophila*. J Eukaryot Microbiol 41, 483–495.
Nilsson JR (1987). Structural aspects of digestion of Escherichia coli in Tetrahymena. J Protozool 34, 1–6.
Nilsson JR, Van Deurs B (1983). Coated pits and pinocytosis in *Tetrahymena*. J Cell Sci 63, 209–222.
Preta G, Cronin JG, Sheldon IM (2015). Dynasore—not just a dynamin inhibitor. Cell Commun Signal 13, 1–7.
Ray K (2008). Chacterization of Paramecium Tetraurelia Ciliary Membrane Plasma Membrane Calcium Pumps and Lipid Rafts. MS Thesis. University of Vermont.
Salisbury JL, Baron AT, Sanders MA (1988). The centrin-based cytoskeleton of *Chlamydomonas reinhardtii*: distribution in interphase and mitotic cells. J Cell Biol 107, 635–641.
Sanders MA, Salisbury JL (1995). Immunofluorescence microscopy of cilia and flagella. Methods Cell Biol 47, 163–169.
Sears JC, Choi WJ, Broadie K (2019). Fragile X mental retardation protein positively regulates PKA anchor Rugose and PKA activity to control actin assembly in learning/memory circuitry. Neurobiol Dis 127, 53–64.
Shamloula HK, Mbogho MP, Pimentel AC, Chrzanowska-Lightowlers ZM, Hyatt V, Okano H, Venkatesh TR (2002). Rugose (rg), a Drosophila A kinase anchor protein, is required for retinal pattern formation and interacts genetically with multiple signaling pathways. Genetics 161, 693–710.
Shang Y, Song X, Bowen J, Corstanje R, Gao Y, Gaertig J, Gorovsky MA (2002). A robust inducible-repressible promoter greatly facilitates gene knockouts, conditional expression, and overexpression of homologous and heterologous genes in *Tetrahymena thermophila*. Proc Natl Acad Sci USA 99, 3734–3739.
Sharma P, Nicoli ER, Serra-Vinardell J, Morimoto M, Toro C, Malicdan MCV, Introne WJ (2020). Chediak-Higashi syndrome: a review of the past, present, and future. Drug Discov Today Dis Models 31, 31–36.
Sievers F, Wilm A, Dineen D, Gibson TJ, Karplus K, Li W, Lopez R, McWilliam H, Remmert M, Söding J, *et al*. (2011). Fast, scalable generation of high-quality protein multiple sequence alignments using Clustal Omega. Mol Syst Biol 7, 539.
Sogame Y, Asami H (2011). Possible involvement of cAMP and protein phosphorylation in the cell signaling pathway for resting cyst formation of ciliated protozoan Colpoda cucullus. Acta Protozoologica 50, 71–79.
Stanke M, Tzvetkova A, Morgenstern B (2006). AUGUSTUS at EGASP: using EST, protein and genomic alignments for improved gene prediction in the human genome. Genome Biol 7(Suppl 1), S11.1–8.
Takahashi Y, Nada S, Mori S, Soma-Nagae T, Oneyama C, Okada M (2012). The late endosome/lysosome-anchored p18-mTORC1 pathway controls terminal maturation of lysosomes. Biochem Biophys Res Commun 417, 1151–1157.
Tan JZA, Gleeson PA (2019). The trans-Golgi network is a major site for alpha-secretase processing of amyloid precursor protein in primary neurons. J Biol Chem 294, 1618–1631.
Toh WH, Tan JZ, Zulkefli KL, Houghton FJ, Gleeson PA (2017). Amyloid precursor protein traffics from the Golgi directly to early endosomes in an Arl5b- and AP4-dependent pathway. Traffic 18, 159–175.
Vogl C, Butola T, Haag N, Hausrat TJ, Leitner MG, Moutschen M, Lefebvre PP, Speckmann C, Garrett L, Becker L, *et al*. (2017). The BEACH protein LRBA is required for hair bundle maintenance in cochlear hair cells and for hearing. EMBO Rep 18, 2015–2029.
Volders K, Scholz S, Slabbaert JR, Nagel AC, Verstreken P, Creemers JW, Callaerts P, Schwärzel M (2012). *Drosophila rugose* is a functional homolog of mammalian *Neurobeachin* and affects synaptic architecture, brain morphology, and associative learning. J Neurosci 32, 15193–15204.
Wang X, Herberg FW, Laue MM, Wullner C, Hu B, Petrasch-Parwez E, Kilimann MW (2000). Neurobeachin: a protein kinase A-anchoring, beige/Chediak-higashi protein homolog implicated in neuronal membrane traffic. J Neurosci 20, 8551–8565.
Wang JW, Howson J, Haller E, Kerr WG (2001). Identification of a novel lipopolysaccharide-inducible gene with key features of both A kinase anchor proteins and chs1/beige proteins. J Immunol 166, 4586–4595.
Wiejak J, Surmacz L, Wyroba E (2003). Dynamin involvement in Paramecium phagocytosis. Eur J Protistol 39, 416–422.
Wiejak J, Surmacz L, Wyroba E (2007). Pharmacological attenuation of Paramecium fluid-phase endocytosis. Folia Biol (Kraków) 55, 95–100.
Wild AR, Dell'Acqua ML (2018). Potential for therapeutic targeting of AKAP signaling complexes in nervous system disorders. Pharmacol Ther 185, 99–121.
Wilson GM, Fielding AB, Simon GC, Yu X, Andrews PD, Hames RS, Frey AM, Peden AA, Gould GW, Prekeris R (2005). The FIP3-Rab11 protein complex regulates recycling endosome targeting to the cleavage furrow during late cytokinesis. Mol Biol Cell 16, 849–860.
Woolworth JA, Nallamothu G, Hsu T (2009). The Drosophila metastasis suppressor gene Nm23 homolog, awd, regulates epithelial integrity during oogenesis. Mol Cell Biol 29, 4679–4690.
Yan M, Collins RF, Grinstein S, Trimble WS (2005). Coronin-1 function is required for phagosome formation. Mol Biol Cell 16, 3077–3087.
Zweifel E, Smith J, Romero D, Giddings TH Jr, Winey M, Honts J, Dahlseid J, Schneider B, Cole ES (2009). Nested genes CDA12 and CDA13 encode proteins associated with membrane trafficking in the ciliate Tetrahymena thermophila. Eukaryot Cell 8, 899–912.